Investigation of Footballs Wakes by Robotic Volumetric PIV

LIU Guan-Li

TU Delft

Investigation of Footballs Wakes by Robotic Volumetric PIV

by

LIU Guan-Li

to obtain the degree of Master of Science
at the Delft University of Technology,
to be defended publicly on Tuesday December 18, 2018 at 13:00.

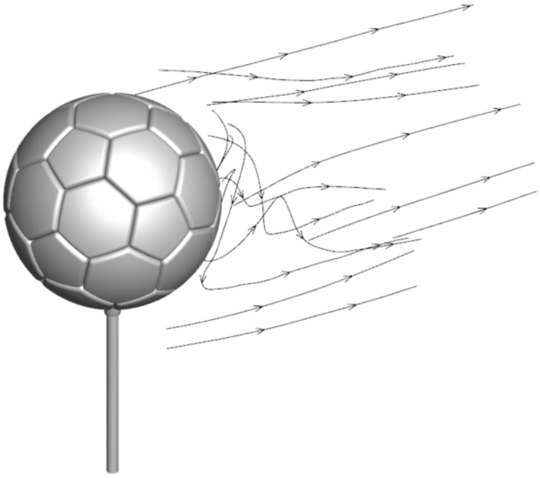

Student number:	4280466	
Project duration:	April 12, 2018 – December 18, 2018	
Thesis committee:	Dr. A. Sciacchitano,	TU Delft, supervisor
	Dr. ir. B. W. van Oudheusden,	TU Delft
	Prof. dr. F. Scarano,	TU Delft
	Prof. dr. ing. G. Eitelberg,	TU Delft

TU Delft

Preface

This report presents the thesis work on the topic of football wake aerodynamics. I am very happy that I could do this, because football is life. So therefore I would first like to thank Andrea Sciacchitano for giving me this opportunity, and of course also for supervising me all along. Also I should thank prof. Scarano here for pointing me towards Andrea Sciacchitano and sports aerodynamics.

What was very nice was that there was a large-scale PIV group, with all students and staff doing large-scale PIV. Occasionally chatting with some of these people and helping each other sometimes was very useful. From the start, PhD student Constantin Jux was always very helpful, and Edoardo Saredi also. Furthermore, it was nice to joke around with fellow MSc students David, Kaustubh and the two Francesco's.

Finally, I would like to thank the technical staff that helped for some preparations of the experiments and providing server access for processing: Nico, Peter, Dennis and Frits. In particular Nico, for also the daily dose of shit talk. Lastly also Colette, for the administrative part.

LIU Guan-Li
Delft, December 2018

Summary

With the introduction of new footballs every World Cup since the past two decades and consequently varying flight behaviour, the aerodynamics of footballs came more into the spotlights. Also scientists started doing many experiments, both in wind tunnels and in-flight, measuring forces and doing wake flow visualisations. However, a volumetric quantification of the wake flow has not been performed until now. The robotic Particle Tracking Velocimtery (PTV) system at the TU Delft is proposed to be used for this purpose, as it could possibly provide a convenient method to quickly and accurately capture the entire wake of a football. If proven to be a suitable system, it could potentially be used in the future as a tool to aid in design or aerodynamic certification of new footballs. The data obtained could also be used for improving Computational Fluid Dynamics (CFD) simulations.

To prove the suitability of the system, a number of experiments were performed in a wind tunnel. The robotic PTV system was used to take measurements in the wakes of two different footballs, at different orientations and at multiple velocities. Additionally, also balance measurements were taken in preparation of the PTV measurements, as well as for checking whether the PTV results made sense. From the results, it was shown that the acquisition system was suitable for taking these measurements. The wakes were accurately captured for subcritical, critical and supercritical Re regimes and wake vortex structures could be seen. The deflections of the wakes also matched the forces from the balance measurements and the acquisition system did not influence the measurements. Also, the expected versatility of the system was proven: only setting up and calibrating once was required.

There was however one issue that came up from the results, which came from the way the ball was fixated. A sting below the ball was used to fix the ball to. This was chosen to be able to easily test multiple orientations, and to not disturb the imaging in the wake. It appeared however that the influence of the sting on the wake flow was too large to neglect and it likely caused the fixation of the wake vortices into a certain orientation. This was concluded indirectly by a comparison of balance measurements: one with the sting from below and one with the sting attached to the ball from behind, the latter setup intended exactly for assessing the influence of the sting.

In order to solve this issue, it was first attempted to find out whether the setup with the sting from behind could be used. Only balance measurements were available for this setup, which were not found sufficient to provide a conclusive answer. Therefore, it is recommended to test in further experiments whether a setup with a sting from behind solves the problem and still allows for useful PTV measurements with a sting right through the area of interest.

Contents

Nomenclature

β	Tomographic aperture	[deg]
θ	Viewing angle with respect to image centre	[deg]
2D	2-Dimensional	[-]
3D	3-Dimensional	[-]
4D	4-Dimensional	[-]
C_D	Drag coefficient	[-]
C_P	Pressure coefficient	[-]
C_S	Side force coefficient	[-]
CAD	Computer Aided Drawing	[-]
CFD	Computational Fluid Dynamics	[-]
CNC	Computer Numerical Control	[-]
CP	Control Point (of the spline describing the outer surface of the ball-sting interface bowl)	[-]
CVV	Coaxial Volumetric Velocimetry	[-]
DOF	Depth of Field	[mm]
FIFA	Fédération Internationale de Football Association	[-]
FSU	Fluid Supply Unit	[-]
g	Gravitational acceleration	$[m/s^2]$
HFSB	Helium Filled Soap Bubbles	[-]
HSL	High Speed Lab	[-]
IPR	Iterative Particle Reconstruction	[-]
OJF	Open Jet Facility	[-]
OTF	Optical Transfer Function	[-]
PIV	Particle Image Velocimetry	[-]
PLA	Polylactic Acid (material used for 3D printing)	[-]
PTV	Particle Tracking Velocimetry	[-]
ppp	Particles per pixel	[-]
Q	Second invariant of the velocity gradient tensor	$[s^{-2}]$
Re	Reynolds number	[-]
STB	Shake-The-Box	[-]
t	Time variable	$[s]$
t_{half}	Flight time for half the parabolic trajectory	$[s]$
t_{end}	Flight time for the parabolic trajectory	$[s]$
TOMO-PIV	Tomographic PIV	[-]
U_∞	Freestream velocity	$[m/s]$
u	Streamwise velocity component	$[m/s]$
USB	Universal Serial Bus	[-]
v_z	Velocity in z-direction	$[m/s]$
v_{z_0}	Initial velocity in z-direction	$[m/s]$
WC	World Cup ball (= Telstar 18)	[-]
z_{max}	Maximum height reached in the parabolic trajectory	$[m]$

List of Figures

List of Tables

1

Introduction

Football is a very popular sport played all around the world, from small scale leisure activity to professional competition in which the stakes are very high, both fame and money. A key factor in this game is the football itself, of which the behaviour has an important impact on how the match progresses. The FIFA (Fédération Internationale de Football Association) being the global governing body of football, has set up standards that footballs should meet to be certified as offical matchballs. [17] These include physical guidelines such as dimensions, weight, water absorption etcetera, but none on aerodynamic behaviour of the balls.

This was never really a problem, as since the 1970s the standard ball has always been shaped like a C_{60} molecule, with twelve pentagons and twenty hexagons (named Telstar). However, with the introduction of the +Teamgeist at the Germany World Cup in 2006, it has become a tradition of the official football supplier of the FIFA to introduce a radically new football design every World Cup. These footballs have different panel shapes and a smaller number of panels: The +Teamgeist (2006) has 14, the Jabulani (2010) has 8, the Brazuca (2014) has 6 and the latest Telstar 18 (2018) has 6. In addition, the panels are now thermally bonded instead of stitched. Leading to rounder balls with less imperfections, the advantage is reduced sensitivity to where the ball is struck. [3] These changes in surface characteristics however also affect the aerodynamics of the balls. In particular this was clear in 2010 with the Jabulani, when complaints of players were common in the media. This was due to the more easily arising knuckleball with this ball: a phenomenon where the ball suddenly changes direction during flight.

This sparked the interest of scientists to investigate football aerodynamics, in particular the past decade has seen an increase in publications on this topic. A literature review on these publications, summarised in Chapter 2, had shown that not much work has been done yet on quantification of the flow field around footballs. It was decided to find a way to quantify the flow field in the wake of footballs, to be able to relate the wake flows of different orientations and balls to the different forces acting. A robotic system for Particle Tracking Velocimetry (PTV)[1] from the TU Delft was used, to show that this system can be used for capturing the entire wake of a football. The objective of this thesis therefore was:

> To prove whether the robotic PTV system currently in use at the TU Delft is a suitable system to measure the 3D flow field in the wakes of footballs to be used in the future as a tool to aid design/certification of new footballs. This is done by using this robotic PTV system to take measurements of wakes of two footballs at multiple orientations in a wind tunnel and relate them to balance measurements of the same footballs.

More details of the objective are provided in Chapter 2 and the working principles of this robotic system are explained in Chapter 3. As mentioned in the research objective, experiments are performed to prove the suitability of the system. The setups and procedures of these experiments are described in Chapter 4. Additionally, also the trajectory simulation that was created is explained here. The trajectory simulation was done to show the significance of the differences in forces measured during the experiments. Then, Chapter 5 discusses the results of all these experiments. Finally, in Chapter 6 a conclusion is drawn on the suitability of the robotic system by considering all these results. Also, recommendations are given for improvement of the application of the system and for possible future research.

---

[1] This system is also often referred to as the robotic volumetric PIV system

2

Research Context and Objectives

In this chapter, an overview is given on the research context of this thesis, namely the aerodynamics around footballs. A description is provided on what is already known from previous research about aerodynamics of spheres and footballs (Sec. 2.1), and which types of data have been collected and what kind of experiments have been performed (Sec. 2.2). Then, from the research gap, Sec. 2.3 sets the objectives of the current thesis work.

2.1. Aerodynamics of spheres and footballs

Section 2.1.1 will first discuss some general aerodynamics of spheres and footballs. Then, Sec. 2.1.2 presents a more detailed look at the influence of the characteristics of footballs, the panels and seams and consequently the effects of different orientations.

2.1.1. General aerodynamics

Footballs, and spheres in general, have a characteristic development of their drag. Figure 2.1 shows an example of C_D vs. Re plots for footballs and a smooth sphere. [19] In the Re range relevant for footballs, three regimes can be discerned. [1] At lower velocities, C_D is relatively high and constant. This is the subcritical regime, where the flow is laminar and when separating at around 82° behind the stagnation point [1] causes a large wake behind the ball. After that, the C_D drops rapidly, a phenomenon known as the drag crisis. This Re regime is called the critical regime. The boundary layer separates around 95°, transitions to turbulent, reattaches, and separates again around 120°. [1] The result is a wake that decreases in size and a reduction of pressure drag, hence the decrease in C_D. At some point, the boundary layer transitions immediately to turbulent instead of forming a laminar separation bubble. This is when the supercritical regime starts, after which C_D increases slowly again.

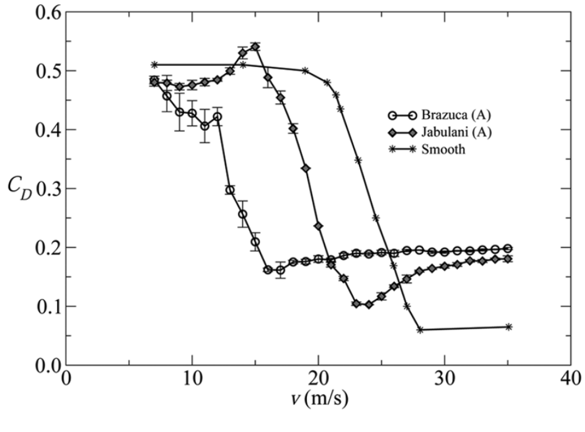

Figure 2.1: Effect of surface roughness on drag curve of a sphere. [19, p.190] Both footballs have a diameter of 0.22m [19] and the smooth sphere has a diameter of 0.2m [1]

The difference between footballs and a smooth sphere, is that footballs have surface characteristics, which cause surface roughness. These are for example seam and/or stitches between the panels, and pimples, roughness elements distributed all over the ball. The effects of surface roughness can also be seen in Fig. 2.1, where the Jabulani and Brazuca, World Cup balls of 2010 and 2014 respectively, are compared to a smooth sphere. As surface roughness enhances transition, the critical and supercritical regimes are reached earlier, therefore the more surface roughness, the more the curve is shifted towards lower Reynolds numbers. The result is that the critcal and supercritical regimes are encountered a lot more frequently during play.

In the subcritical Re regime, the vortex sheet rolls up around the sphere and separates at one point on the sphere, which rotates around the sphere. [2] Also, the wake oscillates in a wave-like motion through the centre of the sphere. [44] However, from the critical Re regime onwards the shed vortex sheet rolls up to form a pair of counter-rotating streamwise vortices. A sketch of this is shown in Fig. 2.2. [44] The vortex pair rotates irregularly around the streamwise centreline and although no clear periodicities were found, on average this happened with a frequency of 0.5 Hz. [44] A more recent experiment using a football reported an average frequency of 1 Hz. [30] Due to this wake flow, spheres in the critical and supercritical Re regime will have unsteady lateral forces.

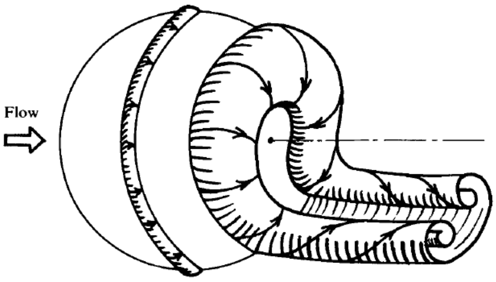

Figure 2.2: Sketch of the supercritical Re regime wake vortex pair. [44]

2.1.2. Seams and orientation

The previous subsection discussed that seams acting as roughness elements can enhance transition and thus postpone separation. However, they also play another more interesting role. When a seam is located close to where natural separation would occur, the separation location shifts onto the seam. An example of this was shown in [30], of which Fig. 2.3 gives a clear illustration using pressure measurements around the ball. In case A, there is a seamline just before 90°, where laminar separation would occur naturally, and this has drawn the separation to it. On the other hand for case B, the seam is far upstream acting as a roughness element, and separation is more downstream than for case A. It should be noted that this was in the critical regime, and that in the supercritical regime this seam effect could not be confirmed from their data. It also mentions that as the seams act as separation triggering source, the separation location is much more fixed, as opposed to for a sphere. [30]

These findings have a number of consequences. Balls with a reduced number of panels and shorter total seam length can have larger differences of surface characteristics at different positions around the ball, leading to larger differences in separation location around the ball compared to balls with more smaller panels, or seams all over the ball. This may generate larger lateral forces. Also the differences between any two random orientations may be larger. Thus, the initial orientation at the beginning of the ball's flight may have a large influence on the trajectory of the ball due to this. This can for example be seen from a comparison between Jabulani and Fevernova (a 32 panel standard Telstar). [5] As a double effect for these balls, the probability of these effects occurring in game increases because with reduced roughness the critical Re regime shifts to higher velocities. This is perhaps another reason, apart from recreating the drag characteristics, to add pimples to the surface as can be seen from the latest few World Cup balls.

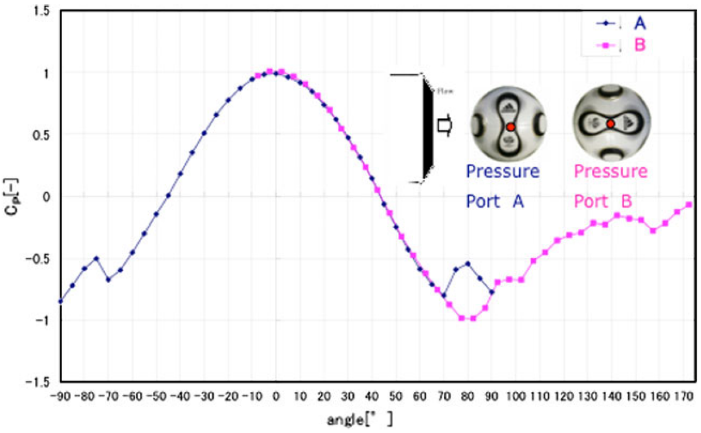

Figure 2.3: Separation angle depending on seam locations. Re = $1.9 \cdot 10^5$ [30, p.38]

A more detailed investigation into influence of seams on separation is provided by [24], where planar Particle Image Velocimetry (PIV) is used to visualise separation. A Cafusa football was used at multiple orientations in a flow of 30m/s, which is in the supercritical regime. Figure 2.4 shows the results of this. This proved that also in the supercritical regime, separation is affected by the positions of the seams, thus orientation of the ball. Moreover, it was indicated that not only the position of a seam in isolation is important, but also the mutual influence of multiple seamlines. Two cases with a seam at the same location can trigger different behaviour depending on the locations of other seams in the neighbourhood.

In figure a), separation occurs halfway between seam 1 and seam 2. The seam is moved to this location in figure b), resulting in separation pushed downstream slightly, 5° behind the seam. And when the seams were closer together as in figure c), separation occurred downstream both, 10° behind the last one, instead of somewhere in between. What they observed was that seam 1 triggered separation, but the flow reattached quickly behind it, then seam 2 separated it completely. (Although it could be that seam 2 has not a major influence here.) In figure d), seam 3 is at the same position as seam 2 in figure c). Now however, there was reattachment at seams 2 and 3, and separation occurred 5° downstream compared to figure c). This shows that the exact effect of seams is even more complex, however the general conclusion that they affect separation, and that therefore trajectory is affected depending on the orientation of the ball is still valid.

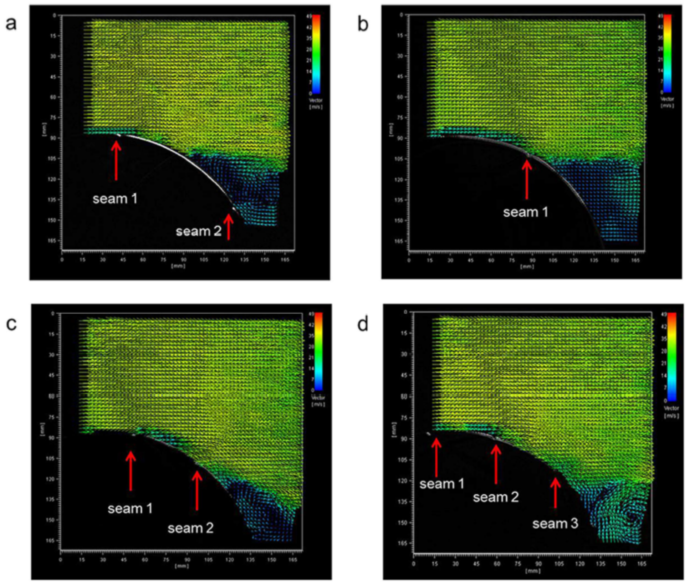

Figure 2.4: "Velocity vectors on the suction side of the soccer balls at U_∞ = 30 m/s." [24, p.5]

2.2. Past experiments

There are three main types of experiments that have been performed: Wind tunnel testing (e.g. [5, 15, 19, 20, 23, 32–34]), free flight testing (e.g. [10, 11, 14, 18, 29]) and CFD simulations ([8, 12, 13]). The advantages of wind tunnel testing are that a controlled environment is used and that it allows for a large degree of control of many parameters, such as velocity and orientations. Disadvantages are that due to the fact that the ball has to be mounted, the unsteady behaviour from a ball in free flight cannot be entirely simulated and influence from the mounting system cannot be avoided. Also, use of wind tunnels is relatively costly. These disadvantages are not present when doing experiments with a ball in free flight. In return, high speed footage is required in order to obtain the force data from trajectory. Depending on the exact setup it is possible to get all data reliably, but is complicated and time-consuming. [21] CFD is the least demanding in terms of physical requirements and allows for full control of parameters. However, a large disadvantage is that transition cannot be predicted well [12, 13]. Even though some general characteristics and data may be retrieved, it is still a very important phenomenon that needs to be simulated correctly to provide reliable results.

In terms of data extraction methods, there are the following: Balance measurements, trajectory simulation and flow measurements. Balance measurements are used to obtain force data in a wind tunnel. For free flight experiments, force data needs to be extracted using trajectory analysis. Trajectory simulation is also done to quantify the effects of the forces measured using a balance. Flow measurements can be visualisations, quantifications or both. Smoke [4] or dust [22] are used to visualise and find the separation angles. Sometimes also, titanium-tetrachloride is used to coat the ball such that smoke comes off the ball itself during flight. [7, 9, 25] To visualise the wake, tuft grids are used in the wake. [29, 30] To get quantitative data, surface pressure measurements are used to find the separation angle [30] and hot wire measurements are done to measure fluctuations of the vortex tail behind the ball [27]. Finally, both visual and quantitative data have been provided by planar PIV measurements, which were used to observe the influence of seams on separation. [24]

2.3. Research objective

From the literature study of what is already known and has been done before, it appeared that not much work had been done on quantification of the flow around a football. PIV had been performed, but only in 2D, and excluding the wake. The robotic Coaxial Volumetric Velocimetry (CVV) system in use at the TU Delft (more details in Chapter 3) could potentially fill this knowledge gap, and in the future be used as a tool to aid design and/or certification of new footballs. One possibility is that this data could serve as validation data for CFD simulations. Improving the performance of CFD is useful, because then the football aerodynamical characteristics can be determined easily early in the design, and iterated as required.

However, it first had to be proven that the system is capable of correctly capturing the flow field. For the purpose of the thesis, the focus lied on the flow in the wake, and as the literature study had shown that ball orientations play an important role in affecting the trajectories of the balls, investigating the differences in wake flow for different ball orientations was also one of the goals. In order to check whether the results made sense and whether the system is suitable for the desired applications, balance measurements were performed along with the PIV measurements.

Therefore, formally this thesis had the following research objective:

> To prove whether the robotic PTV system currently in use at the TU Delft is a suitable system to measure the 3D flow field in the wakes of footballs to be used in the future as a tool to aid design/certification of new footballs. This is done by using this robotic PTV system to take measurements of wakes of two footballs at multiple orientations in a wind tunnel and relate them to balance measurements of the same footballs.

In order conclude whether the objective has been reached, the following subquestions that are used to define 'suitable' have to be answered, by the end of the nine months thesis period:

1. Does the system provide data with sufficient spatial resolution? This is to be determined by:
   (a) Are differences in the wakes for the subcritical, critical and supercritical regimes measured?
   (b) Are differences in the wakes for the different balls and orientations measured?
2. Is it possible to capture the vortical structures in the wakes?

3. Is the wake flow captured correctly by the system, considering if the induced velocities from the flows match the balance measurements?
4. Is the system sufficiently versatile such that the entire wake can be captured by only setting it up and calibrating it once at the start?
5. Is the system non-intrusive, in that the wake flows it measures are not affected by itself?

Using the data from the measurements, the balls and orientations used were also compared to each other. This however was more as an extra, and a check to see whether the results made sense, but was not the main goal of this research.

3

Theoretical Principles of the 4D-PTV System

In this chapter, the working principles are discussed of 4D Particle Tracking Velocimetry system used for the measurements in the wakes of the footballs. First, the general principles of Particle Image Velocimetry (PIV) and Particle Tracking Velocimetry (PTV) systems are briefly introduced in Sec. 3.1. More details can be found in [36], of which this section summarises the main points. Then, the specific system used during the experiments is discussed in more detail. Section 3.2 describes the relatively novel algorithm used for processing the data called Shake-the-box. Section 3.3 presents more the hardware side of the system, also named the Coaxial Volumetric Velocimetry (CVV) system.

3.1. General principles of particle based velocimetry systems

A general 2D 2-component (planar) PIV system is used as an example to illustrate the working principles of PIV/PTV. [36] This is later extended to 3 components and 3D. In terms of hardware, the systems for PIV and PTV are the same, the differences will be discussed later. Figure 3.1 shows a schematic of a PIV system in a wind tunnel. The working principle is simple: seeding the flow with small particles that follow the flow, and deduce the flow field by capturing the movements of the particles. For this, the three main components to note are: the laser and light sheet optics, the illuminated particles and the imaging optics.

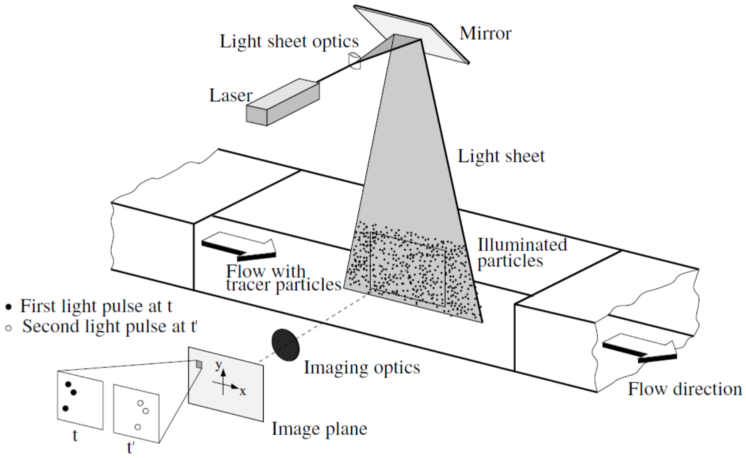

Figure 3.1: Schematic of a PIV setup in a wind tunnel. [36]

Using a laser and lenses, a light sheet is produced that illuminates a plane in the flow. The seeding particles passing through this plane scatter the light, which is recorded by a camera pointing perpendicular towards the illuminated plane. The laser pulses at a certain frequency and the camera images at a certain frequency (not necessarily the same). This results in a series of images. In case of PTV, the seeding density is relatively low, and individual particles are tracked between one image and the next. In case of PIV, the seeding density is somewhat higher and tracking of individual particles cannot be done. In this case, the entire measurement area is divided into so-called interrogation areas. Each interrogation area is compared to the previous time-step and statistical methods such as cross-correlation[1] are used to obtain the displacement of the entire interrogation area in that time-step. Hence, a velocity vector per interrogation area is obtained.

Seeding

For the seeding, there are mainly two concerns: the particles should follow the flow with as little lag as possible, and scatter as much of the light towards the camera as possible. [36] These are traditionally two contradicting requirements, as the first requires particles to be neutrally buoyant and thus as small as possible, whereas the second requires the seeding particles to be larger to reflect more light, as there is a limit to the laser pulse energy that can be reached. [36] As a result, small seeding particles were always used and the laser beam could only be expanded to a limited extent, such that the laser power would not be dispersed too much for sufficient illumination of the particles. This posed a restriction on the achievable measurement volumes. [36]

One way to overcome this problem, is by using Helium-Filled Soap Bubbles (HFSB). [36] By filling soap bubbles with helium, larger seeding particles can be generated that are still neutrally buoyant. An investigation [39] using these bubbles of around 300 μm showed a time response of the order 10 μs. Therefore the HFSB were deemed applicable for use in wind tunnels. For oil droplets of 1 μm the time response was measured around 2 μs across a shock wave. [37] These HFSB are also used in the 4D-PTV system during the experiments of this thesis.

3D and 3 components

The explanation on the 2D 2 component case can be extended for 3D and 3 component measurements. Stereoscopic PIV uses two cameras instead of one, then just like the human sight, depth can be recreated. A more in-depth explanation of the details can be found in [36]. To fully measure 3 components in a 3D volume, tomographic PIV (TOMO-PIV) [16] or 3D-PTV [31] are used. Figure 3.2 shows an example of a TOMO-PIV setup. Four cameras at different viewing angles are used, and by combining the images the real object space can be reconstructed. Similarly to the 2D case, TOMO-PIV divides the volume into interrogation volumes and performs a cross-correlation in 3D. [40] One issue arising from cross-correlation is that velocity gradients are smoothed because spatial averages are taken. Therefore, direct knowledge of particle positions is desired for accuracy, which is the advantage of 3D-PTV. This local accuracy however comes at the extent of lower seeding density compared to TOMO-PIV: order of 0.005 particles per pixel (ppp) compared to 0.05 ppp for TOMO-PIV. [40] The 'Iterative reconstruction of Volumetric Particle Distribution' (IPR) method [47] could reach the same particle density as TOMO-PIV with increased position accuracy, but still had the issue of ghost particles. [40]

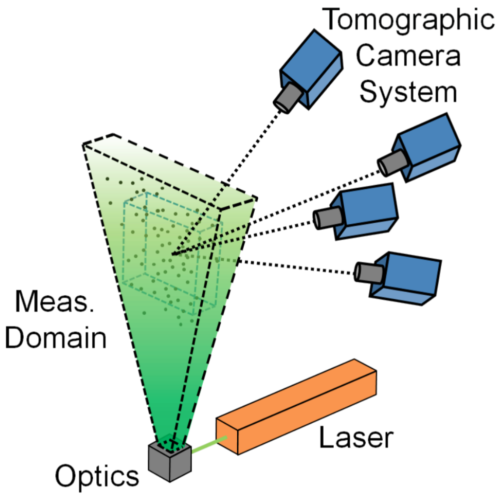

Figure 3.2: Schematic of a TOMO-PIV setup. [28] (Original from [16])

---

[1] Provides a measure of similarity between images.

3.2. 4D-PTV: Shake-The-Box

The Shake-The-Box (STB) algorithm combines the advantages of the aforementioned methods. This section provides a summary of the working principles based on [40]. The algorithm tracks individual particles using methods introduced by IPR, with the seeding density and calibration methods from TOMO-PIV. Additionally, the time-resolved data is used to make predictions on particle distributions from previously calculated track data. Hence, this method has been termed 4D-PTV. The algorithm passes through three phases: the initialisation, convergence and converged phases. These are discussed in short one by one below.

Initialisation phase
The first, typically four, timesteps fall in the initialisation phase. Particles are identified using iterative triangulation and are defined particle candidates. From the distribution of particle candidates, trajectories are identified from these time steps, for example using a method of using search radii. Only then, these tracked particles are considered true particles, as they could otherwise be potential ghost particles. After the second timestep, the search radii could be reduced by creating predictors to estimate the initial velocity field, using the already tracked particles.

Convergence phase
In the convergence phase, the tracks already identified are used to predict the particle positions in the next timestep. Compared to the real image of the timestep, there may be small errors in the particle positions, usually only a fraction of a pixel. These are then corrected using IPR [47], by 'shaking' each of the particles in all three directions, until the residual is minimised. This is done independently for each particle. These newly tracked particles are then linked to their corresponding trajectories and removed from further consideration. From the remaining image, again particle candidates are identified. Similarly to the initialisation phase, these new particle candidates together with untracked particle candidates from previous timesteps are considered to try and find new tracks. Much fewer iterations will be required as much fewer particles are left now. Here, predictors could also be created by using neighbouring tracked particles to reduce the search radii. Then, every following time-step the process is repeated, until nearly all true particles are tracked and a stable state is reached where the number of tracked particles per time-step varies little.

Converged state
In the converged state, the processing is still the same as in the convergence state. In this state, tracks mostly begin and end due to entering or leaving of the measurement domain, instead of ending due to the intensity dropping below a threshold.

Two measures for reducing errors are reduction of ghost particles and outlier detection. The first is done by omitting the camera showing the highest intensity for each particle during particle reconstruction. This reduces the ghost particles tracked, because those mainly take their energy from the peak of one camera. Outliers could occur due to overlap of particles or noise. If the velocity difference with neighbours or deviation from expected trajectory exceeds the thresholds, the particle is deleted.

3.3. Coaxial Volumetric Velocimetry

Even with an improved algorithm as STB, there are still some disadvantages of the TOMO-PIV setup. [41] First of all, a stable structure is required to mount the cameras, which due to requirements on distances between the cameras is typically also rather large. This limits the versatility of the system and makes it a complicated one. Also, extensive calibration is required in order to be able to accurately do a mapping from the images back to real world space. Furthermore, optical access is limited, because on the one hand there is the shadow region from the laser, and on the other hand the shadow region of the cameras. Due to the limited versatility mentioned earlier, it is not easy to move the system around and also capture these regions. This is in particular a problem when the measurement objects have complex shapes.

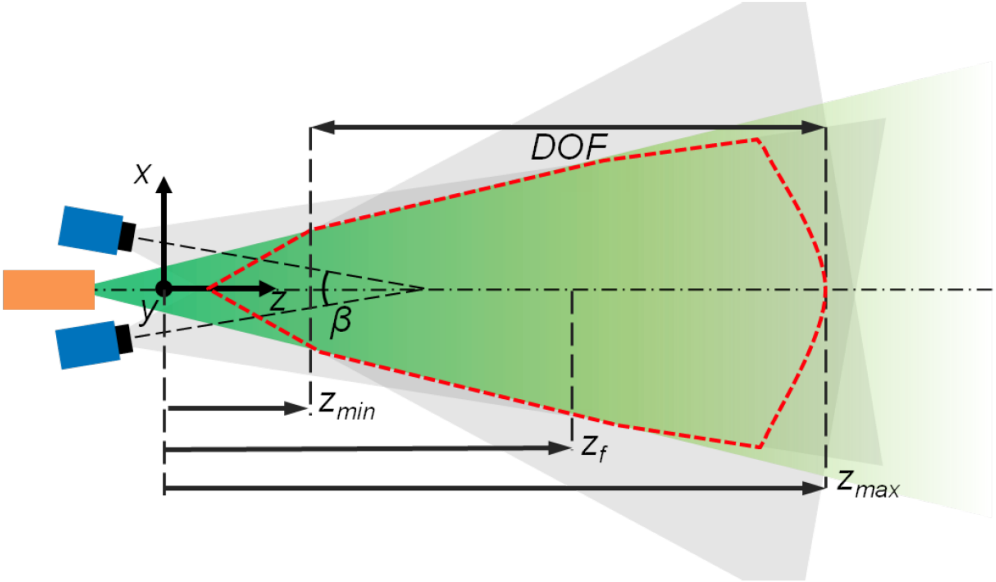

Figure 3.3: Schematic of the CVV system. The grey areas indicate the fields of view of the cameras (blue), the green area indicates the illumination volume of the laser (orange), the intersection of these is the measurement volume, outlined by the red dashed line. The range of depth in focus is indicated by DOF. [28]

To address these issues, a CVV system was proposed in [28]. Figure 3.3 shows a schematic view of this system. The grey areas indicate the fields of view of the cameras and the green area shows the volume illuminated by the laser. The volume suitable for measurements is enclosed by the red dashed line, which is more or less shaped like a cone. In this system, the laser and cameras all have the same viewing direction, hence coaxial. There are a number of advantages to this. First is improved optical access: fewer views are required to capture the complete flow around a complex body. [28] Additionally, more depth can be achieved, which is only limited by the laser power, instead of by the laser sheet thickness when the laser sheet is perpendicular to the camera viewing direction. [28] Also, the system is smaller and more compact. This also provides the opportunity to unite all cameras and laser into one probe, making it much more convenient to move to different views. [28] By then also integrating the probe on an industrial robotic arm, this versatility is exploited optimally. Moving between different views can be achieved easily, therefore large measurement volumes can be realised by stitching these views together. More details on the robotic arm of the system used during the experiments are given in Chapter 4. Recalibration between moving is not required, as the cameras stay at fixed relative positions inside the probe. LaVision[2], the company that developed this concept into a product, which is also used for the experiments of this thesis, has named the probe the MiniShaker, referring to the STB algorithm used for processing the data.

An example of how the versatility of the CVV system combined with a robotic arm allows for convenient large scale PIV measurements is the experiment where the flow field around a full-scale cyclist was captured using an earlier version of the system. Some results of this are shown in Fig. 3.4. [28] The measurement volume comprised a 2 m^3 domain and 450 measurements had to be taken to cover this. It was possible to take measurements at 2 minute intervals by manual operation, and this could be even faster by automating certain parts. It is obvious that the geometry is complex and that there would be many regions that would be difficult to image if this system was not used.

---

[2] `https://www.lavision.de/en/`

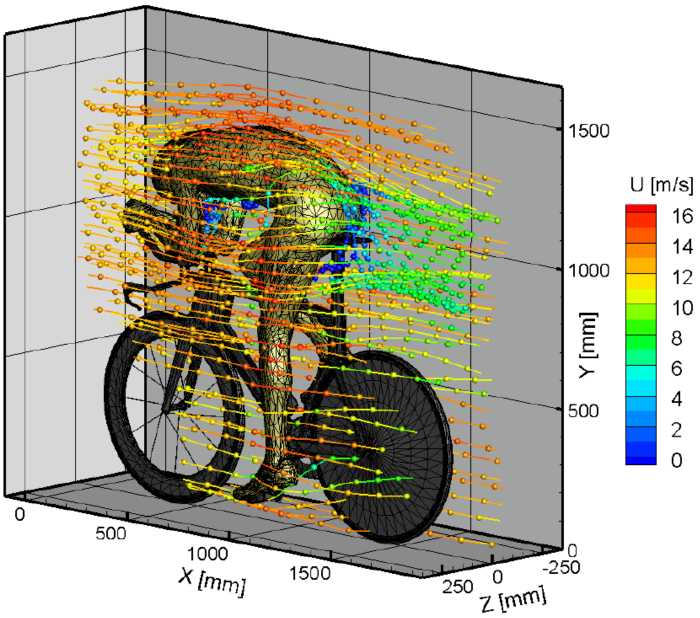

Figure 3.4: "Streamline contours around the full-scale cyclist at $U_\infty = 14 m/s$ coloured by the streamwise velocity component u." [28]

There are however also two issues that arise when applying a coaxial configuration. First, as mentioned earlier the depth of measurement is much larger than for usual TOMO-PIV. In order for particles to be in focus for most of this depth, a smaller aperture is required. [41] This range is called Depth Of Field (DOF) and is also indicated in Fig. 3.3. This smaller aperture however reduces the light that reaches the camera sensors. Combined with the fact that the laser is expanded to the entire field of view of the cameras, it means a large reduction in intensity captured from the reflections of the particles. Use of the HFSB with high scattering efficiency was shown to be able to account for this. [41]

The second issue arises from the fact that the cameras are positioned closer together in this configuration, leading to a smaller tomographic aperture: the angle between the lines of sight from the cameras to the object, indicated by β in Fig. 3.3. The result of this is shown in Fig. 3.5. A smaller tomographic aperture leads to an increase in positional uncertainty in depth when reconstructing the particle, comparing subfigures a) and b). [28] Considering then subfigure c), it is seen that this uncertainty is smaller when the particle is along the edge of one of the sensors. This means that the depth accuracy is higher for particles around the edges of the images. [28] This issue of inaccuracy in depth can be alleviated by averaging large numbers of measurements. [41]

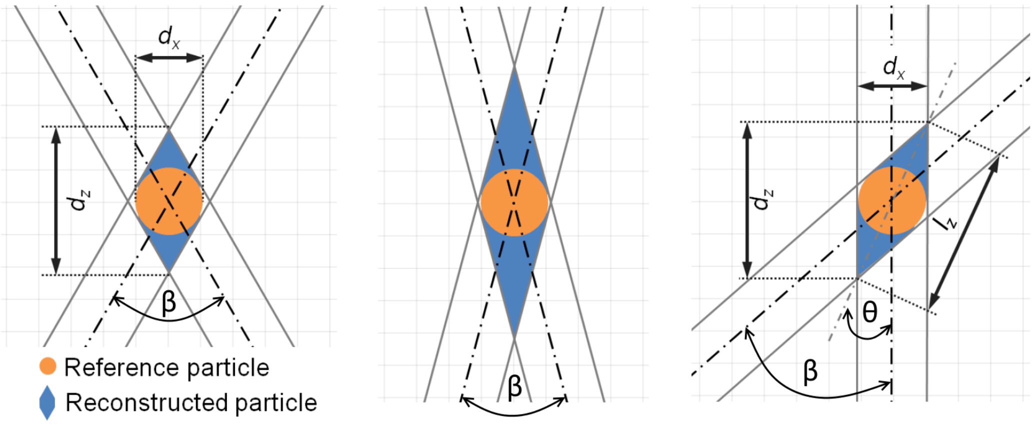

(a) $\beta = 60°$ (b) $\beta = 30°$ (c) $\beta \approx 60°$, $\theta \approx 25°$

Figure 3.5: Comparison reconstructed particles from different tomographic apertures and a different viewing angle. [38]

4

Experimental Setups and Procedures

This chapter presents how the experiments were set up and carried out, also presenting the reasoning behind certain choices and assumptions. As the balance measurements and PTV measurements were both taken in the wind tunnel, being two parts during the same experimental campaign, they are discussed together. Section 4.1 elaborates on the test setup in the wind tunnel and Sec. 4.2 explains the procedures of how data was retrieved during the experiments. The trajectory simulation is a somewhat different type of experiment, thus a separate section 4.3 is dedicated to elaborating on this.

4.1. Setup

This section describes the equipment and setup of the experiments in the wind tunnel. For clarity, they are grouped into the subsections below. The following will be discussed: Wind tunnel, balance and positioning, test objects and mounting, a second setup for balance measurements, PTV system and software used.

4.1.1. Wind tunnel

The experiments in the wind tunnel were performed in the Open Jet Facility (OJF) of the High Speed Lab (HSL) at the TU Delft. The OJF has a large exit compared to the size of a football, almost 3 by 3 metres [35], thus avoiding tunnel blockage effects. It is able to provide wind velocities up to approximately 120 km/h [35] and is therefore very well suited to reproduce the circumstances of a free kick. Fine meshes are used create a uniform inflow for the test section and to reduce turbulence. [35] The turbulence intensity was found to be 0.5% in the freestream, however with a seeding rake (Sec. 4.1.5) in the flow this increased to 1.9%. [28] It should be noted that this was for a smaller version of the seeding rake used currently and the turbulence intensity behind the current seeding rake has not been measured yet.

Figure 4.1 shows a schematic view of the OJF. The large room at the front in which the person is standing is the open test section, and the test object can be mounted where the yellow frame is located.

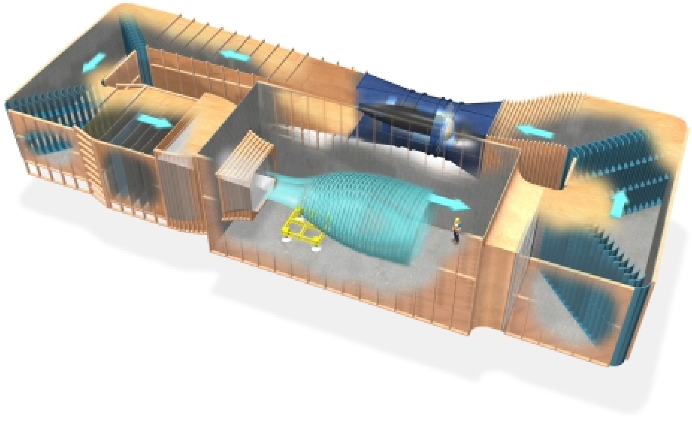

Figure 4.1: Schematic view of the OJF. [35]

In this case, a blue table which could be adjusted in height was placed there, on top of which the equipment and test object was mounted. The height was adjusted such that the test object was located inside the jet, and such that a fresh boundary layer would be formed over the table.

4.1.2. Balance

On top of the blue table a balance was fixated. This was done close to the far end of the table with respect to the tunnel exit, such that the flow past the bubble rake (discussed later) could even out as much as possible. In front of the balance, a construction as shown in Fig. 4.2 was used to prevent the wind from directly blowing onto the balance and disturbing the measurements. The top had a rounded leading edge and a slight negative angle of attack to prevent separation from the top surface. Furthermore, everything was covered in plastic to protect the balance from the bubblestream.

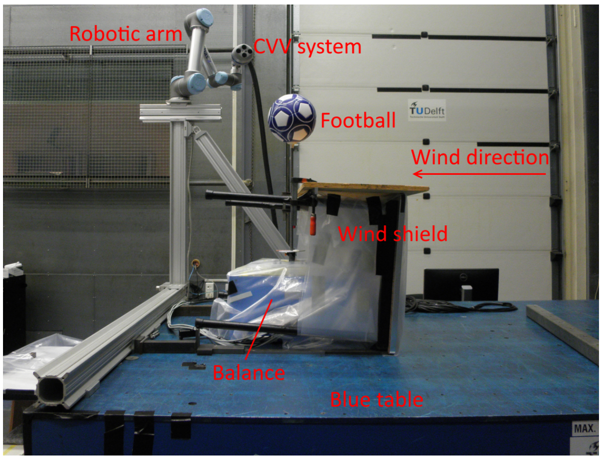

Figure 4.2: Placement of the balance and test object on the blue table.

The balance [6] is a 6-component balance, measuring forces and moments around 3 orthogonal axes. The maximum load in axial (wind) direction is 250 N and for the other two axes 500 N. Therefore, operation will for sure always be far in the safe region. In fact, the small forces are in fact more of a problem. The maximum errors for x, y and z directions are respectively 0.15 N, 1.15 N and 0.8 N. [6] This meant that in particular for the lower velocities the data was not very reliable.

4.1.3. Test objects and mounting

Two footballs were tested during the experiments, the widespread standard Telstar, which can be seen in Fig. 4.2, and the latest 2018 World Cup football, the Telstar 18 with only 6 panels of irregular shapes. Their sizes and weights are listed in Tab. 4.1. Each ball was tested in two different orientations, which were chosen with the aim to achieve the largest difference between the two orientations and thus also get the largest difference in measured forces. For the standard Telstar ball, a symmetrical orientation with the pentagon facing forward was defined as the 0° orientation, and the second orientation was achieved by rotating the ball by 30° to get an asymmetric orientation halfway to the next symmetric orientation. The World Cup ball does not have a symmetric orientation due to its irregularly shaped panels. The 0° orientation was defined as having one of the panels pointing straight forward. The second orientation was reached by rotating the ball by 17° such that the seam between two panels was pointing forward. The balls with the orientations used can be seen also in Fig. 4.3[1]. A compass rose was fixed on the balance to aid determining the angles.

Table 4.1: Sizes and weights of the tested balls.

	Diameter (average) [m]	**Mass [kg]**
Telstar	0.215	0.435
Telstar 18 (World Cup ball)	0.217	0.441

---

[1] The CAD models were downloaded from `https://grabcad.com/library/football-165` and `https://grabcad.com/library/ball-telstar-18-for-fifa-world-cup-russia-2018-1`. They have been modified using Blender (`www.blender.org`)

Figure 4.3: The footballs and orientations used, as seen in reality (top) and the CAD models showing the panels more clearly (bottom). Telstar: 0°, 30°. Telstar 18: 0°, 17°.

In order to suspend the ball in the freestream, a sting was used to position it above the balance while still being fixed to it. To avoid interfering with the flow over the ball, the sting should best be attached to it from behind. [33] However, this was not done for two reasons. First, the wake of the ball is exactly where the PTV measurements would be taken, therefore it was not desired to have a sting there. Second, one of the research aims was to take measurements with multiple orientations of the footballs with respect to the freestream. Rotating the ball around an axis parallel to the freestream would not be useful. The solution could be to use multiple balls, but this would become rather expensive with the world cup ball. The expected consequences of mounting the sting from below have been described in [33]: The values of drag coefficient are higher and the drag crisis drop is less, compared to when the sting is mounted from behind, the reason being that the sting also causes a wake that merges into the wake of the ball.

The diameter of the sting had to be chosen such that it provided sufficient stiffness to minimise vibrations and deflection, but should also remain small to minimise its influence on the flow. In [33], a 20mm sting was used as they say that it is recommended to keep the sting diameter below 10% ball diameter. For the current experiments, a steel sting of 12mm was used, which was found to provide already sufficient stiffness.

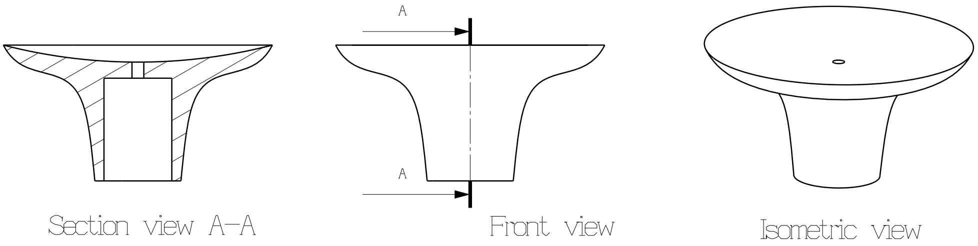

Figure 4.4: The bowl to attach the sting to a football.

To attach the football to the sting, a special part was designed to act as interface. This was required because just the sting cannot be properly attached to the ball, and filling the ball with foam to then drill into the ball as was done in [33] was not desired. First of all to best keep the real characteristics of a football during play, and also to not destroy the ball. Thus eventually gluing was chosen as the method for fixating; epoxy resin was used to provide a strong connection. The bowl used eventually as interface is shown in Fig. 4.4. Multiple other methods using suction and internal mechanical fixation were tried as well, but discarded. The top of the bowl used is a curved surface with a radius of curvature that matched that of the the outer surface of the football. This ensured maximum contact surface area for the epoxy to work on. At the bottom there is a hole to insert the sting; a tight fit ensures that there is no relative movement and rotation during wind tunnel operation, while still allowing replacement of the ball. The remainder of the surface was designed with the aim to provide smooth transitions and the surface was treated by sanding to prevent transition. Each football tested had its own interface attached to it. Appendix A discusses some more details about the bowl including the technical drawings.

Finally, to attach the sting to the balance, an interface plate was made that could be connected to the balance. A lens holder was fixed to this plate and in turn the sting could be inserted and tightened inside the lens holder.

4.1.4. Second balance measurements setup

In a later stage, after the first balance measurements and PTV measurements had already been conducted, it was deemed necessary to take more balance measurements. This was done for two reasons. First, to obtain data at higher velocities which are more representative for shots in real play, to use for the trajectory simulations. Secondly, to investigate the effects of the sting below the balls by also doing measurements using a setup with the sting behind the ball. Due to the lack of PTV system and the gained experience from the previous experiment, the setup was slightly different. In principle, the balance, mounting system, balls and their orientations are all the same, however in this case a black table was put over the balance, providing cover from the tunnel exit onwards, resulting in a much cleaner setup. This can be seen in Figs. 4.5 and 4.6. Figure 4.6 also shows the mounting system used where the ball orientation is still the Telstar 0° orientation but with the sting from behind.

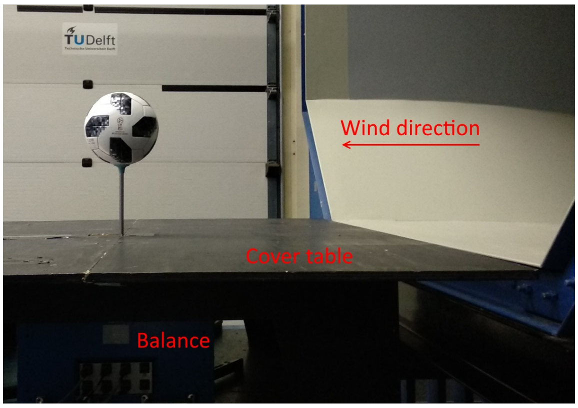

Figure 4.5: Second balance measurements setup showing the World Cup ball with sting from below.

Figure 4.6: Second balance measurements setup showing the Telstar ball with sting from behind.

4.1.5. PTV system

This part describes the hardware used during the experiments.The system for acquiring images consisted of the MiniShaker camera system attached to a UR5 robotic arm [2]. Being attached to the robotic arm allows for imaging at multiple different positions easily, to eventually capture the entire wake. This whole set was from LaVision, that made the camera system. The robotic arm was connected to its power source and controller, that has a tablet attached to it. Using the tablet, the robotic arm could be controlled. By connecting the robotic arm to the computer through a modem, it could also be controlled directly using the computer.

Figure 4.7 shows a close-up of this robotic arm. It has six joints that can rotate ±360° from their neutral position with the rotation directions as shown in the figure: base, shoulder, elbow and three wrist rotations. When fully extended, the reach of the robotic arm is 850 mm. [45] Due the the versatility offered by the six degrees of freedom and the long reach, it was possible to take measurements close by and far away around the football. The translations and rotations of the toolhead with respect to the base are also tracked exactly by the robotic system, which made stitching these images together afterwards not too difficult.

The robotic arm was mounted on a construction made up of X-95 beams[3] that raised it about 1.2m above the blue table, such that the MiniShaker could image both from the side as well as from top looking downwards. Clamps[4] were used to attach the beams to the blue table and each other. See Fig. 4.2.

---

[2] `https://www.universal-robots.com/products/ur5-robot/`

[3] `https://www.newport.com/f/x95-structural-optical-rails-and-carriers`

[4] such as `https://www.newport.com/p/CX95A`

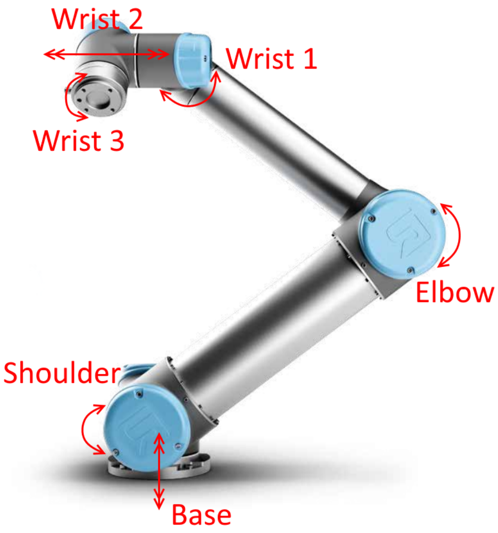

Figure 4.7: The UR5 robotic arm with its six degrees of freedom indicated. Modified from [45]

The MiniShaker has four cameras that are connected to the acquisition computer through USB cables. The cameras can image at a frequency of 821 Hz. Furthermore, the coaxial laser is delivered by an optical fibre in which the laser is focused through the use of lenses. The laser used was the Quantronix Darwin Duo Nd:YLF laser.

Apart from the acquisition components, there is also the seeding system for generating the bubbles, which is controlled by the Fluid Supply Unit (FSU), see Fig. 4.8. The FSU needs to be fed pressurised air and helium, and has a tank for a special soap mixture. Apart from that, there is also a reservoir to store the returning soap that had not been turned into bubbles. During operation, the output pressures of air, helium and soap can be controlled using the control knobs. The soap is pressurised using the pressurised air.

Using four hoses for air, helium and soap in and out, a seeding rake is connected to the FSU. The seeding rake is 0.5 m wide and 1 m long and has 200 nozzles. The internal shape of each nozzle is specifically designed to form the helium filled bubbles. The pressurised air is used to push out the bubbles. To put the seeding rake in the airflow, it was mounted on another construction of X-95 beams. Figure 4.9 shows the seeding rake.

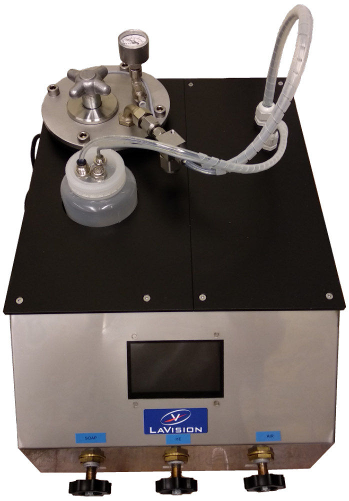

Figure 4.8: Fluid Supply Unit

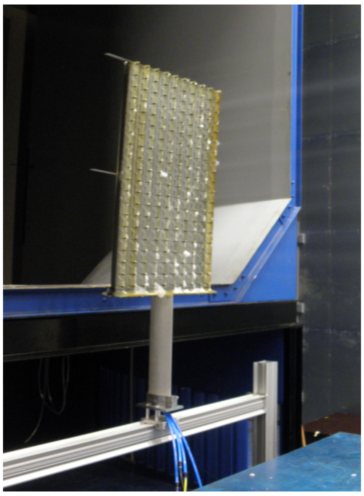

Figure 4.9: Seeding rake.

4.1.6. Software

Balance measurements

For the balance measurements a LabView[5] program was used that had been developed in-house by the TU Delft specifically for the balance. Figure 4.10 shows the front panel of this program. The data for the forces and moments come from the balance, and the remaining values are provided by the OJF. (This only works for measurements in the OJF and the acquisition computer needs to be connected to the OJF network.) Use is very straightforward: Clicking 'Write To File' starts a measurement for the duration of the set measurement time and writes the files afterwards.

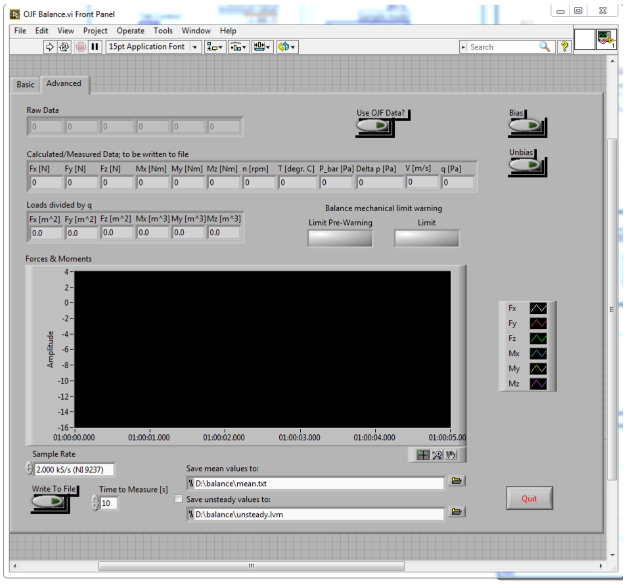

Raw Data

0	0	0	0	0	0

Calculated/Measured Data; to be written to file

Fx [N]	Fy [N]	Fz [N]	Mx [Nm]	My [Nm]	Mz [Nm]	n [rpm]	T [degr. C]	P_bar [Pa]	Delta p [Pa]	V [m/s]	q [Pa]
0	0	0	0	0	0	0	0	0	0	0	0

Loads divided by q

Fx [m^2]	Fy [m^2]	Fz [m^2]	Mx [m^3]	My [m^3]	Mz [m^3]
0.0	0.0	0.0	0.0	0.0	0.0

Sample Rate: 2.000 kS/s (NI 9237)
Time to Measure [s]: 10
Save mean values to: D:\balance\mean.txt
☐ Save unsteady values to: D:\balance\unsteady.lvm

Figure 4.10: Front panel of the LabView program for OJF balance.

For processing of the data, a MATLAB program was created. It provided an easy way to select the desired cases for plotting. Some data alterations were also made. The force measurements from only the sting were taken and a curve fitted through them, this was then used to subtract from the measurements of the footballs, that include the influence of the sting; the measured forces with the wind tunnel off were also subtracted. Also, force coefficients were calculated for non-dimensional analysis.

Additionally, also the instantaneous non-averaged (unsteady) data was considered for comparing the behaviours with the sting from below and behind using another MATLAB script. This was done by performing a frequency analysis for the data, using Welch's method [46], in MATLAB the 'pwelch' function. This method divides the entire signal into (overlapping) segments, and then averages the periodograms of the sections to obtain the final power density spectrum estimate. [46] The advantage of this is that noise is reduced, [46] at the cost of peaks being smoothed out. [26, p. 704] The number of segments used was determined by increasing it until the resulting spectrum had the minimum noise while still retaining all the local peaks that were present when using one segment.

Another thing that was done was using a windowing function on each segment, basically multiplying the signal by a weighting function. The reason for doing this is that the Fourier transform assumes periodicity of the signal, but a real signal is finite and at the edges of the segment, there are discontinuities. The result is noise in frequencies that are not there. A window gives the most weight to the centre of the segment (factor 1), and reduces the weight smoothly towards zero towards both edges of the segment [26, p. 354], thus avoiding the discontinuities. A Hanning window was the type used here. Finally, zero-padding was applied to improve the resolution of resolved peaks. [46]

---

[5] `http://www.ni.com/nl-nl/shop/labview.html`

PTV measurements

For the PTV measurements, a program called DaVis was used, by LaVision. Mainly version 8.4.0 was used, but also an unreleased version was used which had the functionality of Image Particle Reconstruction (IPR) [47]. With this program, the cameras and laser can be controlled for acquisition and it also saves the images taken. Prior to taking images, the cameras also had to be calibrated using this program. Finally, also postprocessing is performed in this program, using the STB algorithm to turn the images into tracks.

Furthermore, two MATLAB scripts that had been developed in-house were used. One program was used to take the track data of different runs taken at different positions and angles and stitch them together into one dataset. These in fact form the final results of the PTV measurements and were visualised using Tecplot[6].

The other MATLAB script was required to actually be able to do the stitching. The reason is that the stitching works by transforming the different views all into one absolute reference frame. For each measurement run, the position of the robotic arm in the base reference frame was required, and then it was a matter of transforming from the camera reference frame to the tool reference frame, then to the base reference frame and the absolute reference frame. However, the transformation from the camera reference frame to the tool reference frame requires the vector from the camera reference frame origin to the tool rotation centre, which is an unknown. As this is hard to measure physically, this second MATLAB script calculates this vector iteratively. [28]

Finally, RoboDK[7] was used to control the robotic arm through the computer. This was very convenient not only because everything could be controlled from one place, but also because different positions of the robotic arm could be saved as targets. So after the desired positions had been determined, the arm could be moved easily back and forth between them. Also, before moving between the targets, a simulation of the required movement could be played before activating the real robotic arm. It could thus be checked if movements would hit the limits of the arm, and by importing CAD models, also collision detection could be performed before moving the real robotic arm.

4.2. Procedures

This section describes the procedures for taking measurements during the experiments. The balance measurements and PTV measurements are treated separately below.

4.2.1. Balance measurements

First, measurements were taken with only the sting, without any ball on top. This data was used to subtract the influence of the sting from the measurements with the footballs. The assumption here is that interference effects can be neglected.

Then, the first ball was placed on the sting, this was the Telstar at the 0° orientation. At each velocity that was measured, 5 measurements of 10 seconds each were taken. First, measurements were taken with the wind tunnel off, to subtract later on. Then, starting at 3 m/s, measurements were taken at 1 m/s intervals. During the measurements, rough plots were made of the drag coefficient curve to keep track of the different regimes, and measurements were at least taken until it was clear the supercritical regime had been reached. This varied between 13 and 18 m/s. Then, the ball was rotated to 30°, and the same process repeated. This was also done for the World Cup ball, for 0° and 17°. For the second campaign of balance measurements, exactly the same was done, except that for all cases, measurements were taken from 3 m/s to 30 m/s at 1 m/s intervals. For processing of the data, the MATLAB scripts mentioned in 4.1.6 were used and have already been described there.

4.2.2. PTV measurements

For the PTV measurements, first some steps needed to be taken to calibrate the system are described. Then the procedure for the actual measurements is elaborated on. Finally, it is explained how the data were processed.

Calibration

First a geometrical calibration was performed. This was done using the LaVision Type 30 calibration plate (see

---

[6] `https://www.tecplot.com/`

[7] `https://robodk.com/index`

Fig. 4.11), which was placed where the football would be located later. The front of the plate was pointing to the side, namely towards the MiniShaker that would later image from the side of the football. Then, the MiniShaker was positioned approximately 400mm from the plate and images of the plate were taken. This was repeated after moving the MiniShaker 200mm closer and further away from the plate. These images were further used in DaVis to perform the calibration to determine how the cameras were positioned. It also set the origin of the camera reference frame.

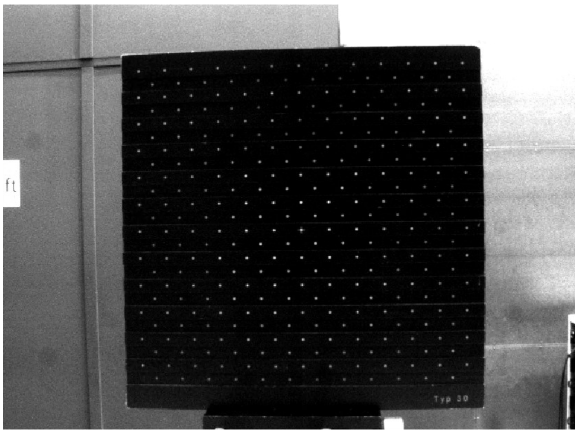

Figure 4.11: The LaVision Type 30 calibration plate as seen through the MiniShaker during calibration.

After the geometrical calibration, a self calibration was performed to further improve the calibration, i.e. to decrease the amount of pixels error. This was done by taking an acquisition of the freestream, with bubbles. The self calibration was then also performed in DaVis. After that, an Optical Transfer Function (OTF) was created, which describes the transformation from the imaging sensor to the real 3D volume. This is required for using STB.

Before doing the measurements, a second type of calibration was also performed first, namely finding the vector between the origin of the camera reference frame of which the origin was set during the geometrical calibration, and the centre of rotation of the robotic arm's tool head. This is required to put all individual measurements correctly in a global reference frame, in other words to stitch different views together correctly.

The calibration was done by first taking images of a calibration pattern at different positions and orientations. The calibration pattern could be anything with 5 to 7 clear dots, during this experiment, the pattern as shown in Fig. 4.12 was used. The images were then processed in DaVis with IPR to obtain the coordinates of the dots for each view. These data were then used in the MATLAB script described in Sec. 4.1.6 to obtain the vector.

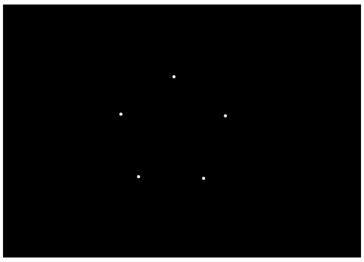

Figure 4.12: The calibration pattern for the rotation centre calibration.

Acquisition

Prior to taking measurements, RoboDK was used to save a number of targets for the camera looking from the side and above that would cover the wake behind the ball. Also, all reflective surfaces in view for these targets were covered with black sheets or plastic. Otherwise, this would cause noise in the data, or saturation in the images, which would lead to areas without data.

From the preliminary results of the balance measurements, it had been decided to do the PTV measurements at 3 m/s, 5 m/s and 9 m/s, because these velocities fall in the subcritical, critical and supercritical regimes. The Telstar was tested at 0° and 30°, the World Cup ball only at 17°, because there was not enough soap and there were problems with the order and delivery of new soap. So a total of 9 cases were tested. For each case the following was done:

The wind tunnel was turned on at the desired velocity, after which the FSU was set to start producing bubbles. Using live mode, the pressures for air, helium and soap were set to produce images that had a desirable seeding density. Then, the MiniShaker was moved through the pre-set targets one by one, and at each target, two measurements were taken of 5000 images each at a frequency of 821 Hz. After all measurements, the FSU was stopped and depressurised to refill the soap tank. The wind tunnel was then set to the next velocity and/or the ball was set to the next orientation and the steps repeated.

Processing

After all measurements had been taken, they needed to be processed to obtain usable data. In all of the images, non-moving unwanted objects were in view, and there were still reflections also recorded on the images. These signals should not be taken into account for further processing, so these were removed first. This was done by using a Butterworth filter that removes signals that stay on the same place all the time [42], see for example Fig. 4.13. However, the Butterworth filter works less well when the object moves. The balls moved back and forth slightly, so even after applying the filter, reflections of the ball would show up periodically. For these cases, a Gaussian smoothing filter was applied first, which by smoothing the reflection signals, slightly compensated for the moving back and forth. This improved the resulting images, though could not entirely remove the unwanted reflections. Small areas at the balls surfaces therefore had some noisy data, but these would not affect the data of the rest of the wake, which was mainly considered.

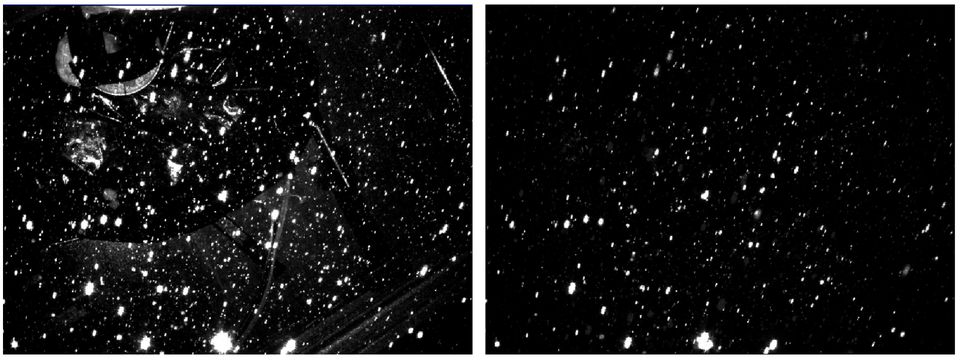

Figure 4.13: Raw image and the same image processed with the Butterworth filter.

After the preprocessing had been done, the resulting images could be used to calculate the tracks by processing them using STB. [40] An example of the result is shown in Fig. 4.14. Some of the parameters that had to be set are intensity threshold and maximum voxel shift. Intensity refers to the brightness of the pixel as recorded by the camera sensor measured in counts, and the threshold sets the minimum number of counts before it is considered a particle to use in the algorithm. For most runs 10 counts was used, or 5 counts in case a Gaussian smoothing filter was applied, since that lowers the overall intensity. In some cases where the seeding was too full, 15 counts were used to reduce wrong particle coupling and thus noise.

A voxel is the 3D equivalent of a pixel. Between every two images, the particles shift a certain distance in the image depending on the wind velocity. The maximum voxel shift is the largest distance the algorithm will search to couple particles between consecutive images. Thus the value had to be set such that it was large enough that the particle falls within the search radius on the next image, but small enough to avoid spurious vectors: a particle on one image coupled to the wrong particle on the next. An estimation for a good choice of value was made as follows: The field of view of the real world in millimetres and the corresponding image in voxels could both be seen within DaVis. Thus the number of millimetres represented per voxel could be calculated. Also, the maximum shift in millimetres between two images could be calculated by dividing the wind velocity by the imaging frequency. When dividing this by the amount of mm/voxel, the result is the voxel shift between two images. The value chosen as maximum voxel shift was selected slightly higher than this (a few voxel) to allow for some acceleration over the ball to be captured, but this was not expected to be much since the measurement area was mainly the wake of the ball. Choosing a too high maximum voxel shift could lead to wrong couplings.

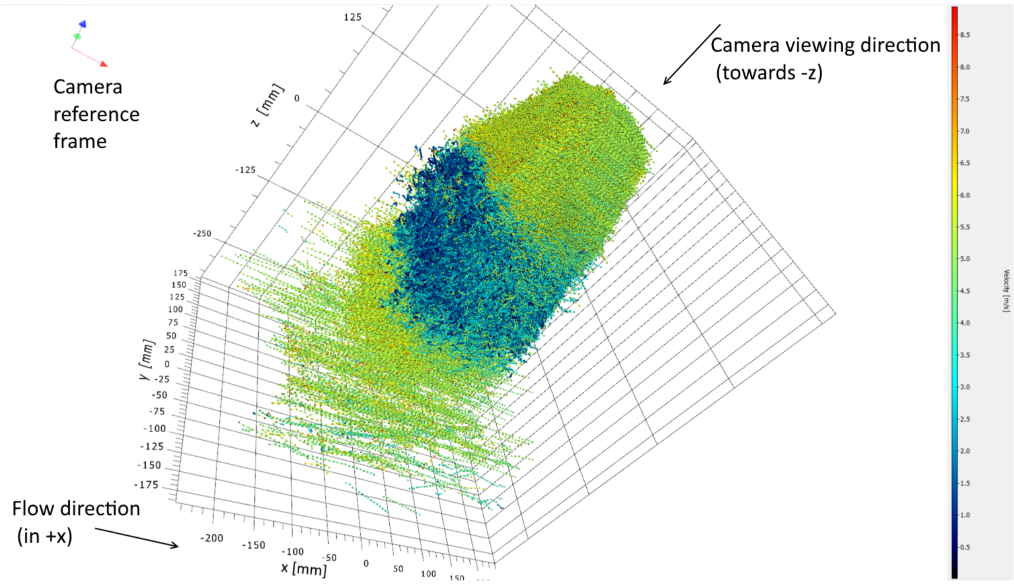

Figure 4.14: Resulting tracks after STB processing in DaVis.

The resulting track data were also written to a data file. These data files were used in a MATLAB program along with information on the positions of the robotic arm and on transformations between the reference frames. One at a time, the desired runs from the same ball orientation and wind velocity were set in the program and binned. Meaning that the total measured volume was divided into bins, and the track data for all selected runs was divided over the correct bins to calculate the velocities for each bin. A bin size of 25mm was chosen and 75% overlap between the bins was used. The results of this binning are presented in Chapter 5.

4.3. Trajectory simulation

In order to quantify the effects of the differences in forces and thus to be able to make a statement on the importance of the experimental results obtained, a trajectory simulation was created using MATLAB. In this simulation, the force data from the balance measurements were used, and thus the trajectories of different ball orientations could be compared. The following assumptions and simplifications were made for this simulation:

1. Lift ignored, since the focus is to quantify effects of side forces. The data is probably also not too reliable, due to the presence of the sting. Drag and gravity are included.
2. The football does not spin.
3. Assume yaw and pitch angles are negligible, meaning that the forces used all correspond to the initial orientation.
4. Drag acts in the flying direction, side force to the side (parallel to goalplane) and not perpendicular to flying direction.

The simulation allows to set initial elevation angle and velocity, after which the trajectory is simulated and stops when either the ball hits the ground or passes the goal plane. The trajectory is numerically integrated for each time step, and this is looped until one of the conditions is violated. The time step used was 0.001 s, because further decreasing the timestep showed no relevant improvement in terms of physical distance. The validation of the program that is described later in this section is what was used to check this. Further, the integration scheme used was the trapezoidal rule, because an explicit scheme was required and this was more accurate than simply forward integrating and still very simple to implement in MATLAB.

For each timestep, the velocity at that timestep is used to obtain the drag and side forces from a fit through the drag and side force balance data. Combined with the mass of the ball, the accelerations are then obtained, and the numerical integration is then applied to obtain the velocities and displacements.

Validation
Two cases were used during the creation of the simulation to validate. First simulating a free fall, then also simulating a parabolic drag free trajectory. These could easily be compared to analytical solutions and validated that the program worked correctly and the numerical integration scheme was sufficiently close. Also, they helped in removing bugs and were used to find the required timestep. Figures 4.15 and 4.16 show visually these validation cases. In the following, a large number of decimals is left shown, in order to be able to show the difference between exact and numerical solutions.

For the free fall test case, a free fall of 1.5 seconds was simulated. This simulation time is considered sufficient, since any reasonable shot on goal will arrive within that time. Using a gravitational acceleration of $g = 9.81[m/s^2]$, the exact analytical solution gives a fall of 11.036 m and the numerical simulation gives a fall of 11.051 m. A difference of 0.015 m was considered sufficiently small to not have a noticeable influence in play.

For the parabolic trajectory test case, an initial velocity of 20 m/s and a launch angle of 30° was used. Two points were compared with the analytical solution, the point of maximum height and the point where the ground is hit again. To calculate the point of maximum height, Eq. 4.1 was used.

$$v_z(t) = v_{z_0} - 9.81 \cdot t \tag{4.1}$$

Setting this to zero and applying the initial vertical velocity of 10 m/s yields for the time elapsed halfway and at the end of the trajectory:

$$0 = 10 - 9.81 \cdot t \Rightarrow t_{half} = 1.019[s] \Rightarrow t_{end} = 2.038[s] \tag{4.2}$$

From the numerical integration, the values are 1.018 s and 2.038 s for halfway and end of trajectory respectively. Using these values, the x distances covered are 17.656 m and 35.312 m from the analytical solution, and 17.650 m and 35.32 m from the numerical solution. The maximum height reached was calculated by integrating the vertical velocity up to the half-way time:

$$z_{max} = \int_0^{t_{half}} v_z(t)\,\mathrm{d}t = 5.0968m \tag{4.3}$$

The numerical solution yielded 5.0968 m, and for the end point of the flight where the exact solution is a height of 0 m, the numerical solution gives -0.002641 m. These results are summarised in Tab. 4.2 Again, the differences between exact and numerical solutions have shown to be sufficiently small.

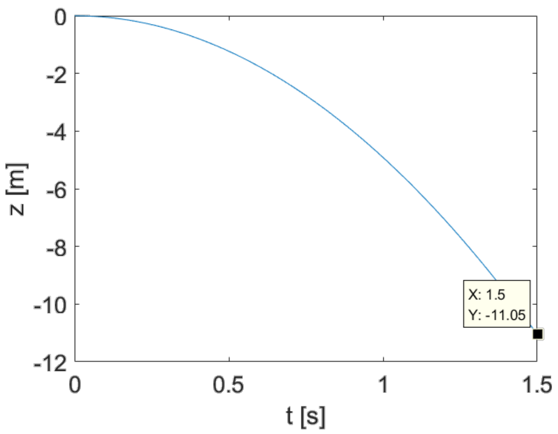

Figure 4.15: Validation of trajectory simulation using free fall test case, using $g = 9.81[m/s^2]$ and a simulation time of 1.5 s.

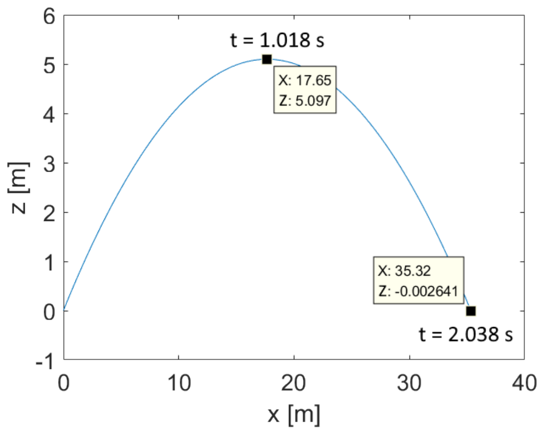

Figure 4.16: Validation of trajectory simulation using drag-free parabolic flight test case. Using $g = 9.81[m/s^2]$, initial velocity of 20 m/s and initial launch angle of 30°.

Table 4.2: Summary of the validation of the parabolic trajectory test case.

Variable	**Units**	**Exact solution**	**Numerical solution**
Halfway time	[s]	1.019	1.018
Halfway distance	[m]	17.656	17.65
Halfway height	[m]	5.0968	5.0968
Final time	[s]	2.038	2.038
Final distance	[m]	35.312	35.32
Final height	[m]	0	-0.002641

5

Results

In this chapter the results of the balance measurements, PIV measurements and trajectory simulation are presented. The balance measurements and PTV measurements are discussed in Sec. 5.1 and Sec. 5.2 respectively, in which the results are interpreted and explained, and interesting details are highlighted. Section 5.3 then relates the results from the balance and PTV measurements. Finally, Sec. 5.4 shows the results of the trajectory simulation.

5.1. Balance measurements

As explained in Chapter 4, two balance measurement campaigns were performed: one in concurrence with the PTV measurements, and another more extensive campaign with a cleaner setup. The results of the measurements in concurrence with the PTV measurements are discussed later in Sec. 5.1.3. First, the results of the balance only measurements are presented, for the best comparison of characteristics between different orientations and balls. These data are also used for the trajectory simulation. The results are shown in Figs. 5.1 to 5.4. The legend names refer to the balls used and the orientations, as described in Chapter 4.1, where WC is the World Cup ball. The lift force is not shown, because the side force is used as the measure for comparing the lateral forces for the different orientations and balls. The lift data is also considered less reliable due to the sting breaking the up-down symmetry. In the results shown here, the contribution of forces acting on the sting has already been removed.

5.1.1. General observations

Considering the drag data, in Fig. 5.1 the expected parabolic increase of drag with velocity can be seen. Also, transition is visible from the changes in slopes. The same data is shown in non-dimensional form in Fig. 5.2. Clearly, the laminar region, the drag crisis and the subsequent slow increase in C_D in the supercritical regime can be seen. Strangely, there is a slow decrease in C_D in the supercritical regime and only for much higher Re does C_D seem to slowly increase again for the Telstar at 0° and the World Cup ball at 17°. This could perhaps be explained by considering first another observation: the fact that the values of C_D are relatively high and the drop in C_D is limited. As was explained in Chapter 4.1, this is due to the positioning of the sting below the ball, shown in [33]. Potentially, for higher Re this effect of the sting being located below the ball become smaller, and as such the values of C_D slowly creep towards the values they would be without influence from the sting. The results of the measurements with the sting mounted behind a Telstar at 0° orientation for comparison are shown in Fig. 5.5. These confirm that with the sting from behind, the values of C_D are lower and the drag crisis causes a larger drop, which agrees with literature. [33] The supercritical regime now does not show a decline in C_D anymore, and so it seems plausible that it was due to the effect of the sting from below.

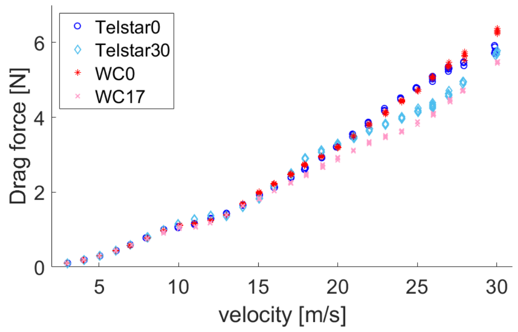

Figure 5.1: Balance measurements drag versus velocity.

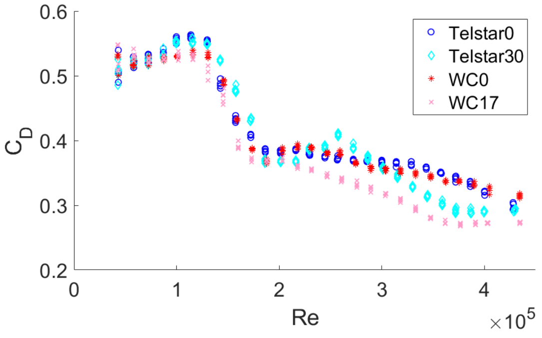

Figure 5.2: Balance measurements C_D versus Reynolds number.

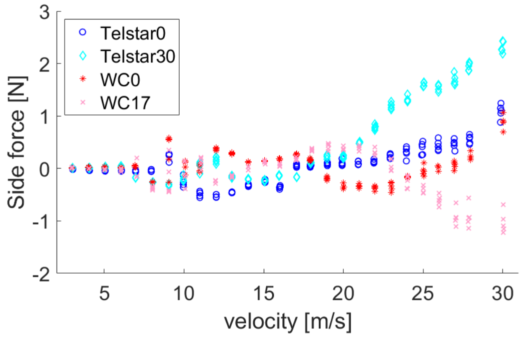

Figure 5.3: Balance measurements side force versus velocity.

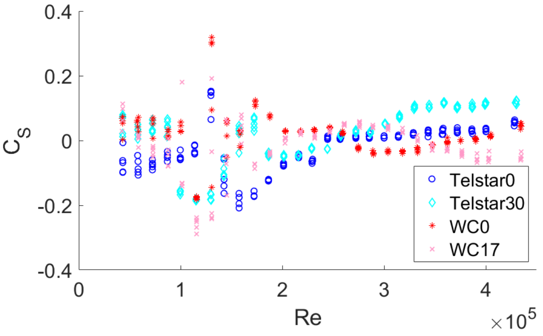

Figure 5.4: Balance measurements C_S versus Reynolds number.

Figures 5.3 and 5.4 show the results for the side force measurements. The side forces do not seem to have very predictable patterns, but it does look like there is a pattern per *Re* regime. In the subcritical regime, the forces are small and steady. This is clearly different in the critical regime, where the forces are suddenly multiple times larger, seem to be a lot more unsteady considering the spread of datapoints for the same velocities, and fluctuate a lot for varying velocities, changing sign at least once. The supercritical regime is then characterised by less fluctuating side forces, but slowly they grow larger and larger in a certain direction for each case. In terms of C_S, here the fluctuations are much smaller and the magnitudes all stay within 0.2.

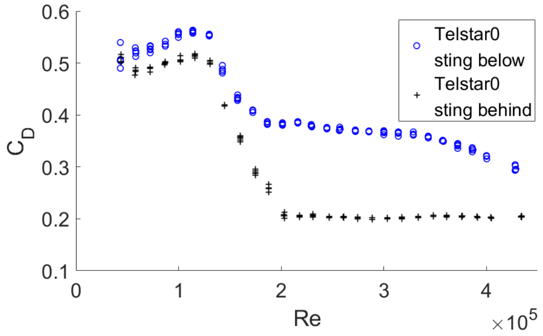

Figure 5.5: Balance measurements of Telstar 0° orientation with stings from below and from behind, C_D versus Reynolds number.

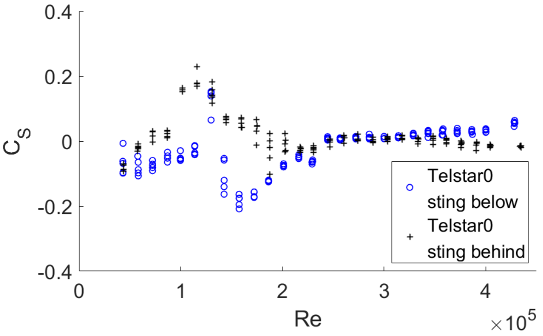

Figure 5.6: Balance measurements of Telstar 0° orientation with stings from below and from behind, C_S versus Reynolds number.

Comparing the sideforces for the Telstar with stings from below and behind, a clear difference is seen between their values of C_S in the critical regime. There does seem to be a similar pattern of increasing to positive values until the critical regime, then decreasing towards zero again. Only for the case with sting from the rear the values do not become that high and quickly decrease again, ending up with an increase towards zero in the supercritical regime, when both cases behave the same. However, for the highest velocities, they start to develop differently again. In itself, it is not strange that there are differences. Apart from the different setups, it cannot be expected that the balls were placed in exactly the same way, and the balls were likely also not exactly the same.

5.1.2. Comparison of orientations/balls

Comparing the two orientations of the Telstar ball, the orientation at 30° has a drag crisis at slightly higher *Re*, after which the C_D is lower in the supercritical regime. This is apart from the strange peak near $Re = 2.5 \cdot 10^5$, of which it is unknown what has caused it. Similarly for the World Cup ball, the orientation at 17°, which is the more asymmetric one, has clearly lower C_D values than the 0° orientation. A possibility is that for the more asymmetric cases, a larger part of the seams are in the wake, causing less friction drag which in the supercritical regime has a larger contribution. However, this has not been investigated in-depth.

Comparing both balls to each other, the World Cup ball at 17° has the lowest C_D values in the supercritical regime. The expectation was that the World Cup ball would indeed have the lower drag in the supercritical regime, because it has fewer panels and the seams are less pronounced. However this seems not to be true for the 0° orientation, which even ends up with higher C_D values than the Telstar ball at 30°.

A number of observations can be noted for the side forces. The cases of more symmetric orientations for both balls have side forces closer to zero, which makes sense. The differences in side forces for the two orientations of the Telstar ball are smaller than the differences between the two orientations of the World Cup ball when considering the highest Reynolds numbers. For the World Cup ball, even the sign is different between the two orientations. This is an expected result, because with more panels, the differences in surface characteristics between two orientations is smaller than when there are fewer panels.

5.1.3. Measurements concurrent with PTV

The results of the balance measurements done during the PTV measurement campaign are shown in Figs. 5.7 to 5.8. A number of differences with respect to the pure balance measurements can be observed. Due to the seeding rake and less clean setup introducing turbulence in the flow, transition has been much advanced, the subcritical regime can hardly be seen, perhaps a glimpse of it for the Telstar ball at 0°. It was then however assumed that 3 m/s lied at the end of this regime. Trying to obtain data at lower speeds would not make sense anyway, as both the wind tunnel and balance would not operate properly at these low velocities and forces. The data indeed showed to be unreliable when it was tried. From these data, it was chosen to use 3m/s, 5m/s and 9m/s for the PTV measurements, in order to capture data in all three *Re* regimes. Going higher than 9 m/s would still provide data in the supercritical regime, but complicate the PTV measurements needlessly. These velocities are highlighted in the figures by vertical lines.

The side force do not grow larger and larger for increasing velocities as seen before. However, those were encountered at higher velocities than for which measurements were taken during this campaign, which is probably the reason they do not appear here yet.

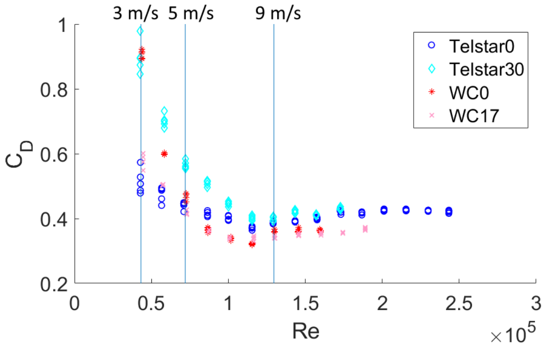

Figure 5.7: Balance measurements C_D versus Reynolds number. (PTV)

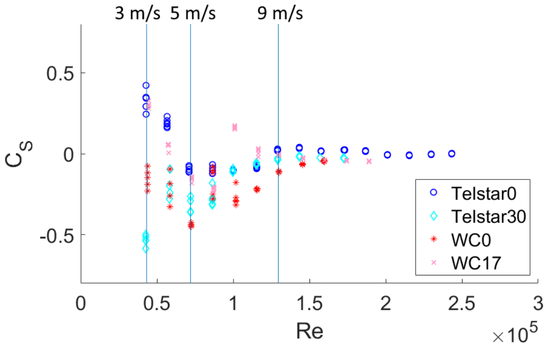

Figure 5.8: Balance measurements C_S versus Reynolds number. (PTV)

5.2. PTV measurements

Figures 5.9 to 5.11 show some results of the wake flow fields, visualised by plotting different slices. The airflow is in the positive x direction. In the figures, the footballs are positioned at the actual position with respect to the flow and in the relevant orientation, and their centres are defined as (0,0,0). The planes of the slices pass through y=0 and z=0, and through x=120mm which is just behind the balls. The values of the streamwise velocity components are plotted, normalised by the respective freestream velocity, as well as a number of streamlines.

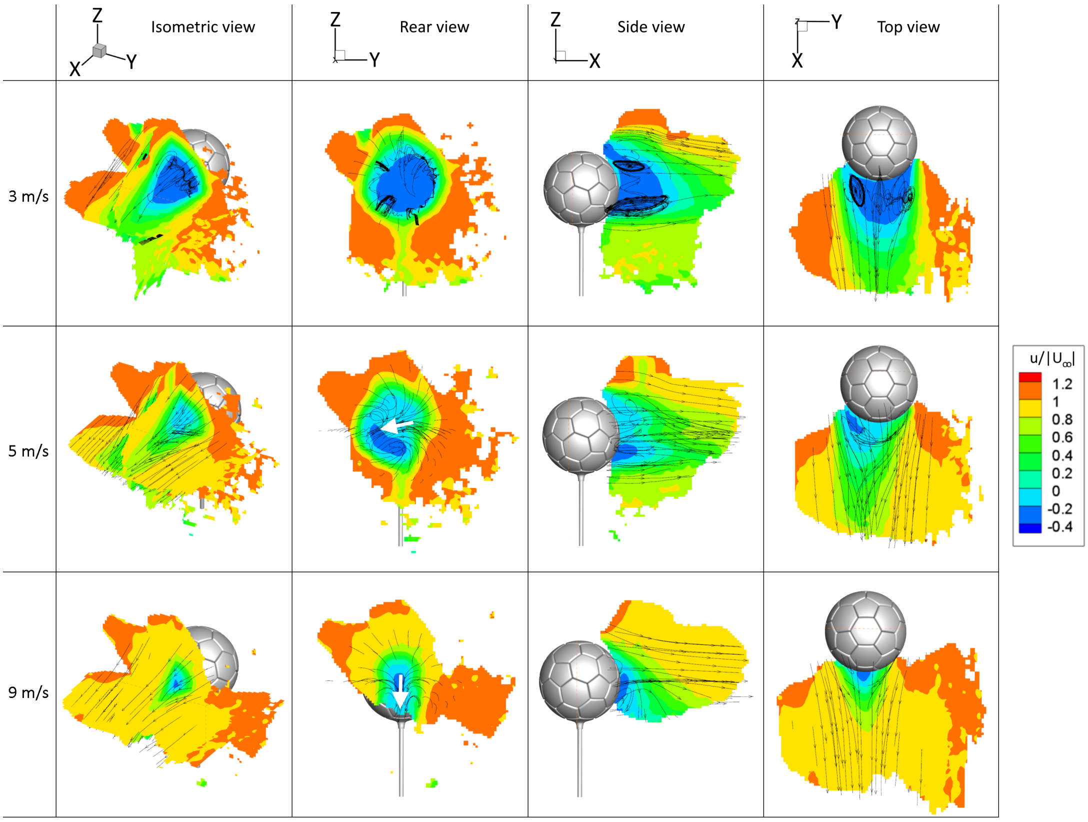

Figure 5.9: Normalised velocity fields of the Telstar football at 0°. White arrows indicate directions of vortex pair induced flow.

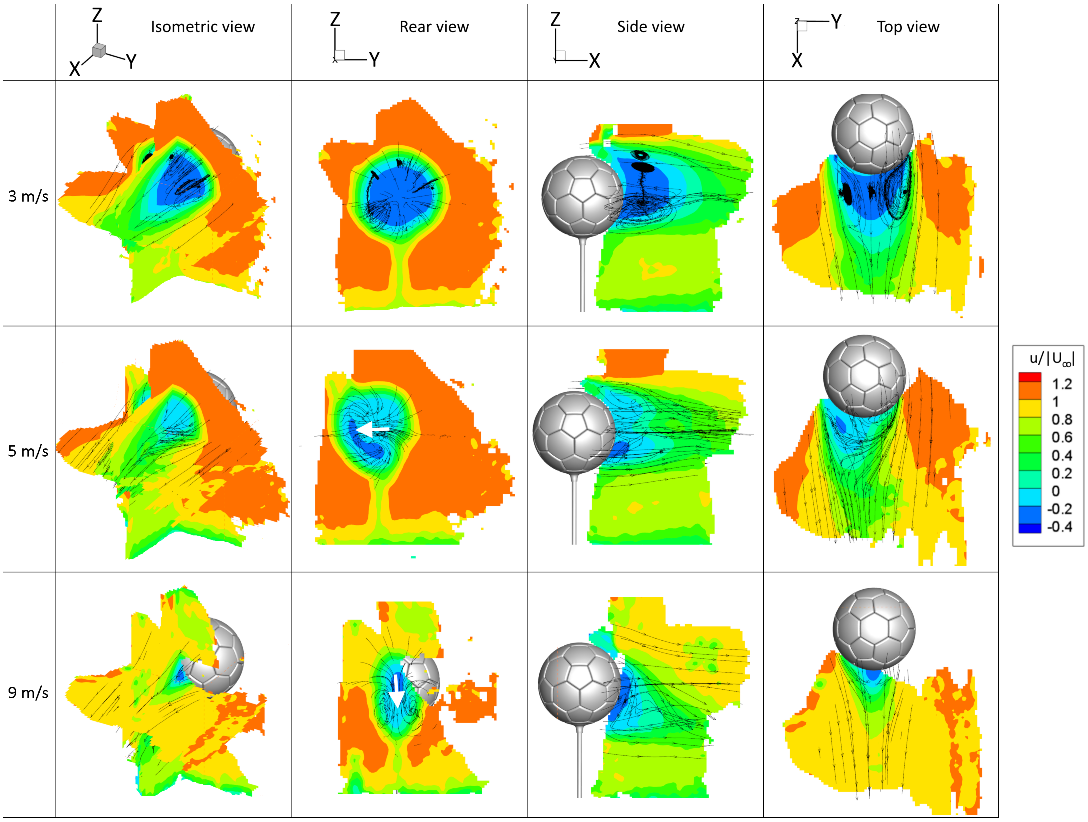

Figure 5.10: Normalised velocity fields of the Telstar football at 30°. White arrows indicate directions of vortex pair induced flow.

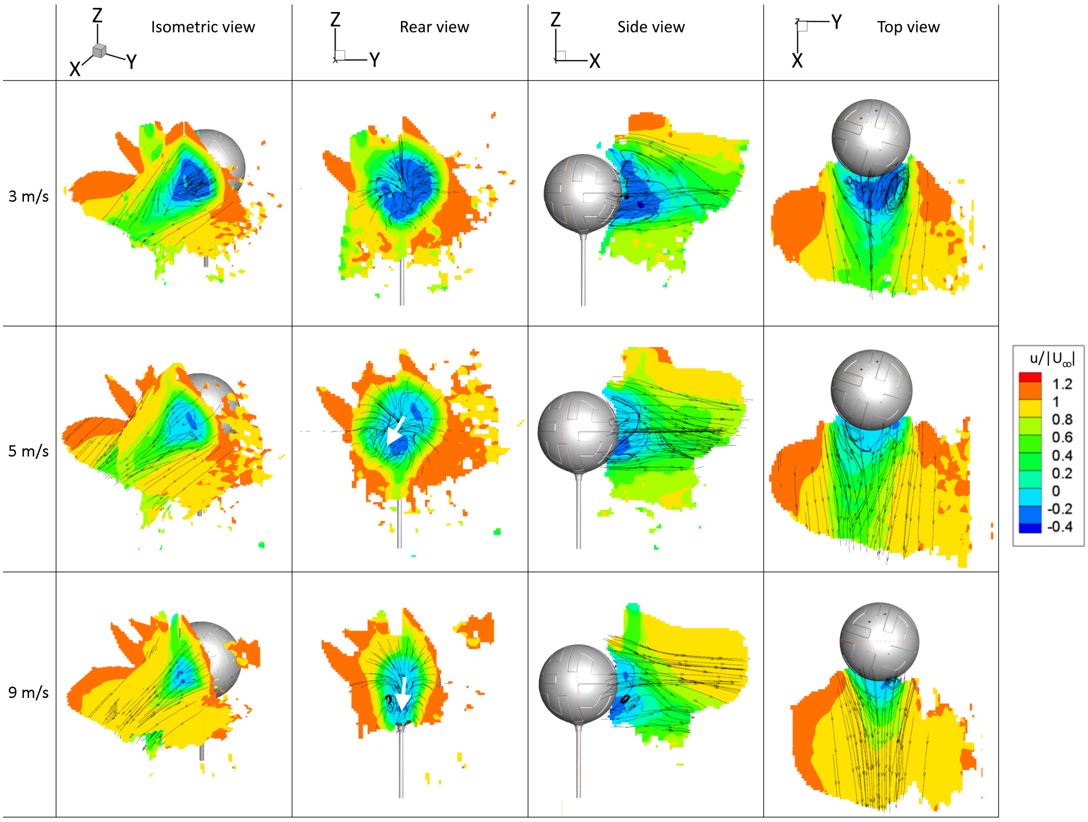

Figure 5.11: Normalised velocity fields of the World Cup ball at 17°. White arrows indicate directions of vortex pair induced flow.

5.2.1. General observations

Wake sizes

A number of things can be observed from these results. First, it is clearly seen that the consequence of transition is captured: the wakes for the 9m/s cases (in the supercritical regime) are much smaller compared to the others. Figures 5.12 to 5.14 show a more detailed comparison of this by overlaying for all three test velocities the contour lines that indicate where the axial velocity is half that of the freestream. From these it can be seen that the subcritical wakes extend three times further downstream than the supercritical wakes.

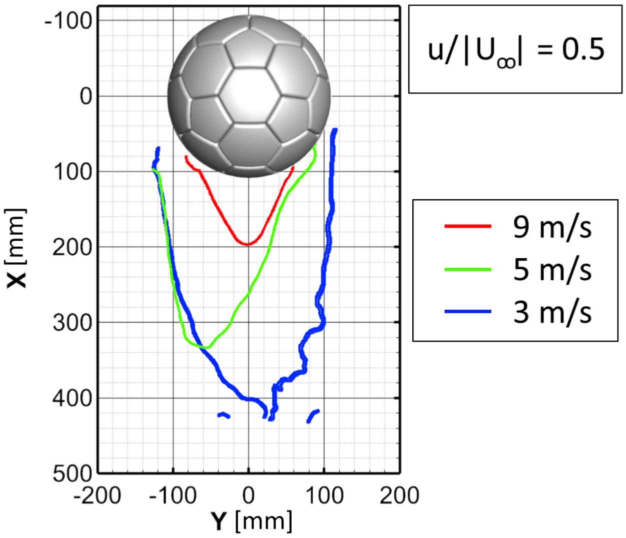

Figure 5.12: Contour lines of $u/|U_\infty| = 0.5$ at 3 m/s, 5 m/s and 9 m/s for the Telstar 0° case.

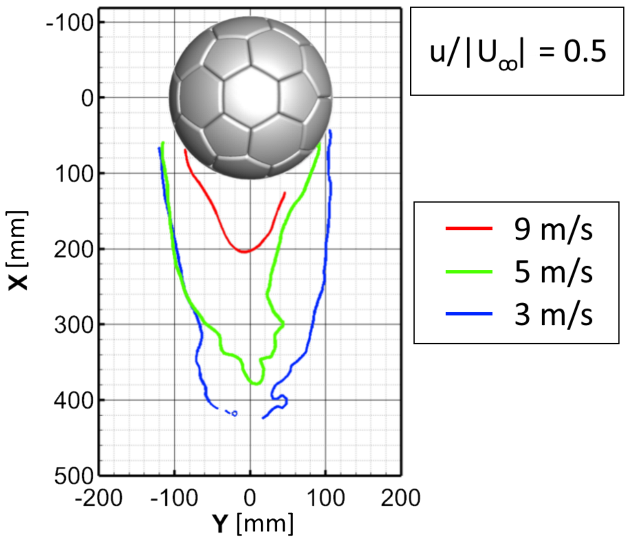

Figure 5.13: Contour lines of $u/|U_\infty| = 0.5$ at 3 m/s, 5 m/s and 9 m/s for the Telstar 30° case.

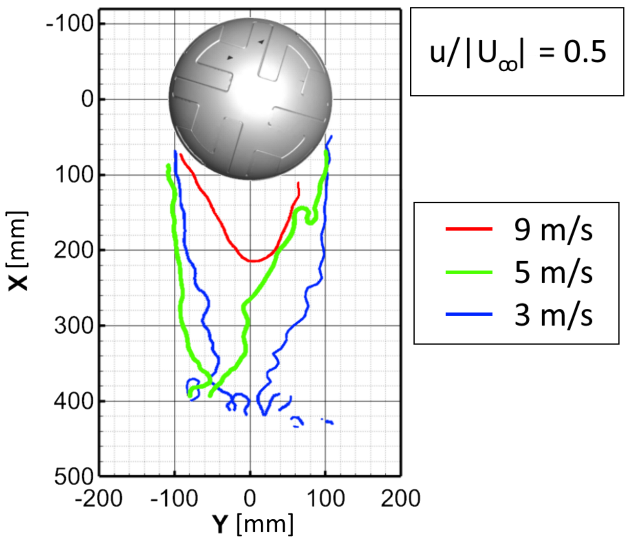

Figure 5.14: Contour lines of $u/|U_\infty| = 0.5$ at 3 m/s, 5 m/s and 9 m/s for the World Cup ball 17° case.

Figure 5.15 shows an estimation of the separation angles for all cases, measured with respect to the front stagnation points. They are summarised in Tab. 5.1. The wakes were defined as the regions where the normalised streamwise velocities were below one.

Table 5.1: Overview of the estimated separation angles from the PTV data.

Case	Separation angle left [deg]	Separation angle right [deg]
Telstar 0°		
3 m/s	<120	<114
5 m/s	<122	117
9 m/s	129	132
Telstar 30°		
3 m/s	<121	<104
5 m/s	<122	114
9 m/s	125	N/A
World Cup 17°		
3 m/s	<120	<109
5 m/s	<123	<122
9 m/s	125	N/A

The angles shown in the figure refer to the angles that the red lines on the wake sides make with respect to the vertical lines. The slanted lines are drawn to where the wakes as defined start. However this was not always possible, because the separation angle was outside the available data. In those cases, the lines were drawn to where the data stopped, and in the table it is indicated that the separation angles are less than those values. There were also two cases for which the available data was too far from the surface to make a proper estimate.

Overall they match with what is expected from literature. In the subcritical *Re* regime, laminar separation was reported in literature at 82°. [1] Although this is not possible to observe from the results, it can be seen that the wakes are slightly larger than the ball cross-sections, as was also observed in another experiment with a football. [30] In the supercritical cases, separation was reported to be around 120° [1] or '123 to 147°' [44].

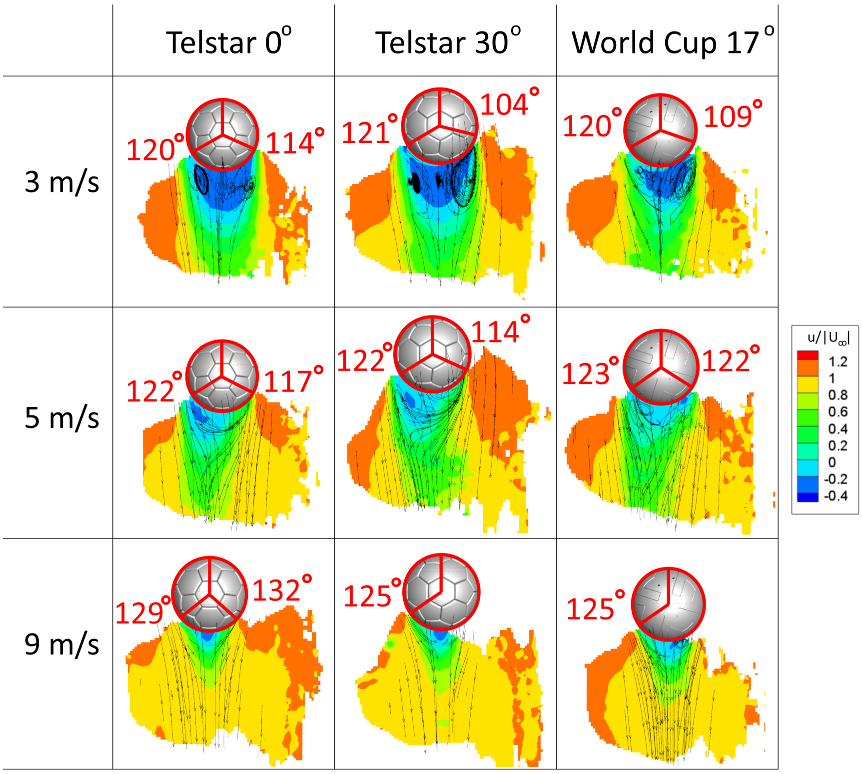

Figure 5.15: Estimation of separation angles of all cases and velocities using the top view.

Wake vortex structures
A second observation from Figs. 5.9 to 5.11 is that by looking at the streamlines, it can be seen that in the subcritical cases, there is no streamwise vortex pair and only a roll-up of the vortex sheet, whereas from the critical regime on there are streamwise vortex pairs. This is in agreement with what has been described in literature. [30] By plotting iso-surfaces of $Q = 300s^{-2}$, this vortex sheet roll-up and wake vortex pair can be visualised, shown in Fig. 5.16. It can be clearly seen how the wake evolves from the subcritical to the supercritical *Re* regime. Figure 2.2 from literature showed a sketch of this for the supercritical *Re* regime, but now this structure is reproduced using real quantitative data.

Furthermore, it can be seen that for the cases that there is a vortex pair, the wake is directed in the direction of the induced velocity of the vortex pair. In the figures this direction is indicated by white arrows. It seems that the directions of vortex pairs and wake deflections are closely related and cannot be viewed separately. Strikingly, where the directions vary between the cases in the critical regime, in the supercritical regime the vortex pairs all have an induced velocity pointing downward.

What is interesting to note, is that these results were obtained using time-averaged data, thereby even using multiple measurements that were taken at very different time instances. For these flow structures to come up so unambiguously, it must mean that there had been preferred orientations of the flow. Referring back to [30], it had been reported that "a vortical wake structure almost randomly rotates with an average interval of 1 s and sometimes disappears", no preferred orientation had been observed. (Taneda [44] reported for a smooth sphere no clear periodicities, but a mean frequency of 0.5 Hz for the changes in rotations.) The current results were all obtained using at least 25000 images, which would cover at least 30 periods. Therefore the question arises what has caused the preferred directions seen in the current results.

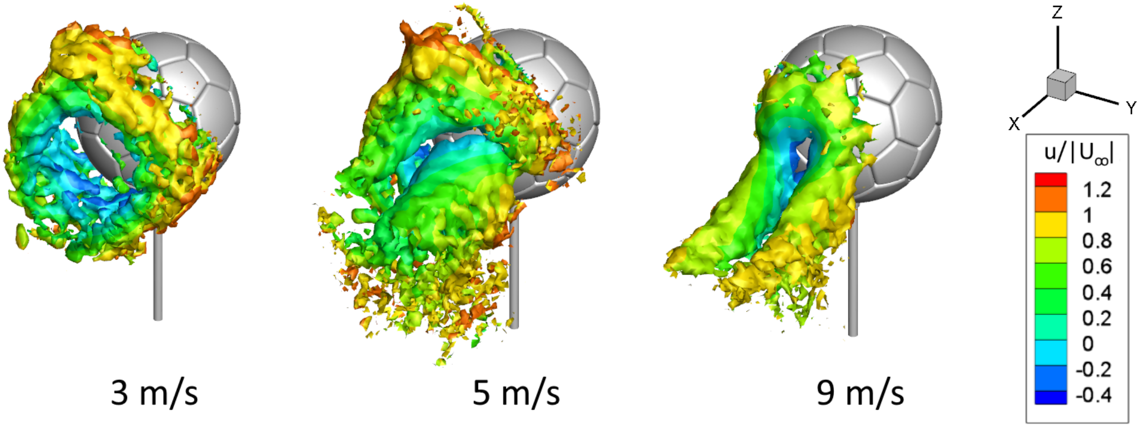

Figure 5.16: Vortex sheet roll-up to wake vortex pair from the subcritical to the supercritical *Re* regimes, visualised by plotting iso-surfaces of $Q = 300s^{-2}$ coloured by freestream-normalised streamwise velocity component u. The Telstar 0° case is shown.

Multiple factors are thought to play a role, including some that are not supposed to, either with one being dominant or as a combination. First, the surface characteristics probably affect how the wake and vortex pairs are oriented. Surface characteristics can be the orientations of the panels, but also imperfections in surfaces and roundness. Seeing differences in the wake due to these surface characteristics is what is aspired. However, the preferred orientation of the vortex pairs could also be influenced by factors coming from the experimental setup: On the one hand the sting mounted below the footballs, on the other hand the MiniShaker and robotic arm that disturbed the flow field.

The reason why the sting being below the football is thought to influence the direction of the vortex pair, is that in all cases of 9 m/s flow, the induced velocity of the vortices is directed downwards, which is unlikely to be a coincidence. The explanation would be that the wake of the sting draws the flow down, resulting in the given orientation of wakes and vortex pairs. This however cannot be the full story, because it does not explain why the wakes are then deflected into varying other directions for the 5 m/s cases. It is reasoned that there the wake of the sting is not strong enough to lock the wake of the football in a downward direction, whereas at higher velocities the pressure difference is sufficiently large to do so.

To further investigate this issue, two measurement cones were processed again, but this time each measurement was not processed as a whole, but divided up in sets of 500 images, each set therefore spanning

0.6 seconds. This was done to try and see whether rotations of the vortex pairs could be observed. Even if overall a preferred direction stands out, this can happen; there could be different orientations as long as for most of the time the vortices are in the dominant orientation. Figures 5.17 and 5.18 show these partial binnings for the Telstar 30° 5 m/s and 9 m/s respectively. One thing they prove is that rotations can hardly be spoken of, only very minor fluctuations around the preferred vortex pair orientation are present at most. Now returning to the discussion of the influence of the sting, it is interesting that for both the 5 m/s and 9 m/s cases, the vortices are more or less locked. Previously, it was posed that the locking was due to the sting, and that the influence of the sting had to be lower for 5 m/s to make sense. Therefore it was expected that there would be at least some rotations for the 5 m/s case, but there are not. This does not mean that the sting has no influence, but it means that the influence of the sting is not proven. It could still be that a low non-zero influence from the sting, in combination with other factors causes a locking of the vortex pairs in a different direction than downwards.

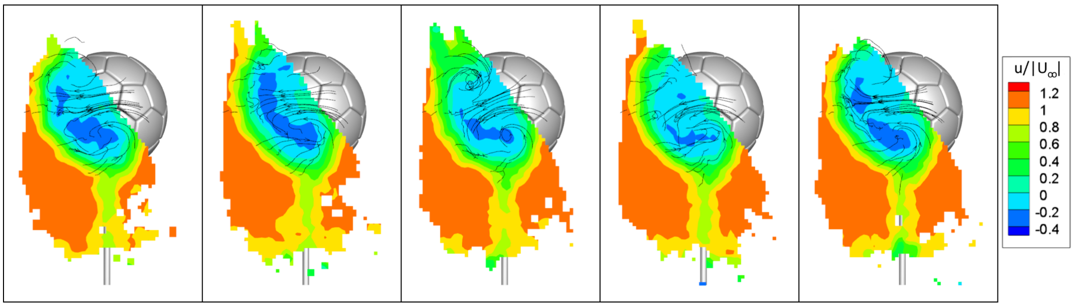

Figure 5.17: Binnings of one measurement cone for the Telstar 30° 5 m/s case, per 500 images.

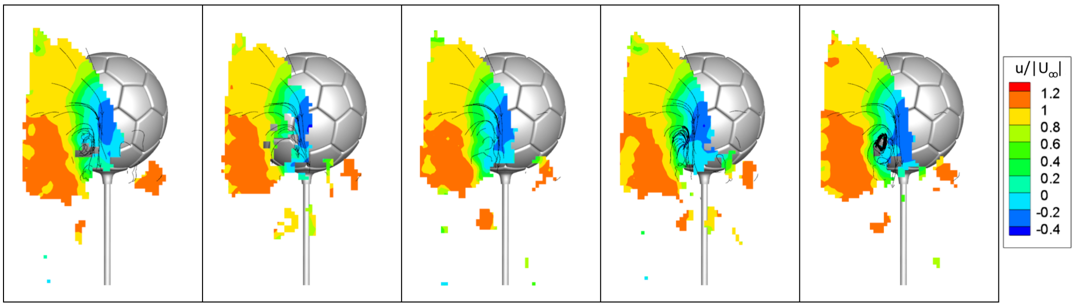

Figure 5.18: .Binnings of one measurement cone for the Telstar 30° 9 m/s case, per 500 images.

If the sting does affect the orientation of the vortices, and its influence is less dominant at lower velocities, the contributions of other effectors become more apparent, namely the balls themselves and/or the PTV system. To explain why the PTV system is thought to possibly affect the direction of the wake, one should note that for the 5 m/s cases the induced velocities all point towards the left (negative y) direction, which is where the system is located. While a strong indication, it can however not be said with certainty that this causes the bias towards the left, because the MiniShaker took images from multiple locations to the left and top of the wakes (seen from behind), which were then all averaged into the results presented. In the case the MiniShaker and robotic arm have a dominant effect, it would be more likely that no clear direction would show up.

To try and understand how large the effect of the acquisition system is on the direction of the wake, binning was also performed on two cones separately for the Telstar 30° 5 m/s case, which were taken at two different positions: one from the side and one from the top. These results showed only little difference in the orientations of the vortex pairs, see Fig. 5.19. Therefore it seems likely that the acquisition system is not responsible for drawing the vortices into one direction. It could however still be possible that the difference is small due to the combined effect of different factors, such as the influence of the sting. But even in that case, it would then mean that the MiniShaker and robotic arm have a limited influence.

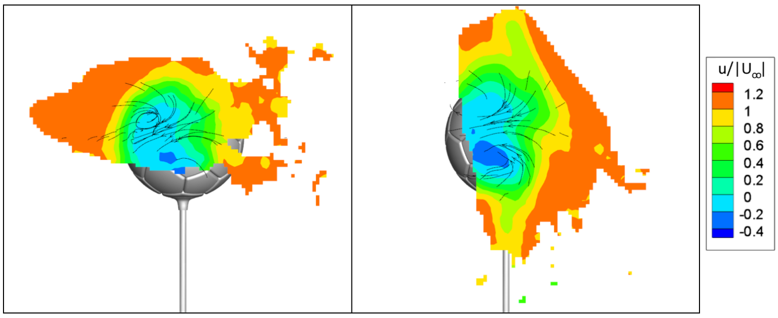

Figure 5.19: Two measurement cones for the Telstar 30° 5 m/s case, one from the side and one from the top.

5.2.2. Comparison of orientations/balls

When comparing the different orientations and balls, the most striking is that there is little difference between the wakes. The only real difference is the direction of the vortex pair for the 5 m/s measurements. When considering that the factors outside the balls are in principle the same, these differences could be attributed to the differences in surface characteristics of the cases.

However, at the moment it is not immediately clear from the results how the seam patterns would have affected the wakes. The fact that the wakes of the Telstar ball with 0° and 30° orientations look similar was not expected. For the 0° case, which is symmetric with respect to the xz-plane, it was expected to have a wake that is also symmetric around the xz-plane. One explanation could be the imperfections of the ball, such as panels not stitched together perfectly edge-to-edge or non-sphericity. The second option could be external influences as mentioned before (sting/acquisition system). In order to make a conclusive statement, it is wise to first investigate the exact issues arising from the external factors.

5.3. Relating balance and PTV measurements

For the drag, the results of the balance measurements and PTV measurements are in well agreement. For increasing velocities, the wakes decrease in size and the drag coefficients decrease in value.

More interesting is the comparison with the side forces. For the cases where a wake vortex pair is present, there should be a resulting force opposite to the direction of the flow induced by the vortex pair. For the supercritical *Re* regime cases, the vortex pairs are all directed downwards, and therefore side forces close to zero are expected. Looking back at the side force coefficients in Fig. 5.8, this is indeed the case. For the critical *Re* regime cases, the induced flows point towards the negative y direction, and as such forces in the positive y direction are expected. By taking into account that the balance reference frame has z pointing downward and y pointing to the left as viewed from the rear, negative side forces are expected. This indeed matches with the measured forces. For the subcritical regime, the balance measurements show side forces of similar magnitude. However this cannot be discerned from the PTV results, all the wakes at 3 m/s look more or less symmetric. Possibly with a larger wake, much smaller deflections that are barely visible correspond to the same forces.

Going back to the discussion of the influence of the acquisition system, the fact that the results from the balance and PTV measurements match, again points to a limited effect of the system. This is because during the balance measurements, it was retracted as far as possible away from the football. In both cases, the vortices seem to be oriented the same way. For a definitive statement, a PTV measurement at a velocity that gives a positive sideforce from the balance would be needed to exclude chance. Unfortunately this is not available at the moment.

On the influence of the stings

The other potential external influence mentioned was the sting below the balls. An attempt was made to understand how much that influence was in locking the vortex pair into a certain orientation. This was done by comparing the balance measurements data from the cases of the Telstar at 0° orientation with the sting from below and from behind. The first thing is to also compare the lift data of both cases, shown in Fig. 5.20. When the sting is below the ball, the vortex pair was seen to have a downward induced velocity in the supercritical regime and C_S was close to zero as shown in Fig. 5.6. It is now also shown that as expected negative lift was registered by the balance.

When now turning the attention to the case with the sting from behind, it was shown previously that C_S was similar to that of the case with the sting from below, at least for the early supercritical regime. When now comparing the lift, two observations can be noted. The first is that there is a large difference between the cases, the second is that at the same time, they do have the same sign. This means that also in case of the sting being behind the ball the vortex pair (mainly) has the downward orientation, but that if the sting is below the ball, the wake is drawn downward much more strongly. Therefore, it is clear that the sting behind the ball has an unacceptable influence on the wake flow.

Considering the observations from the point of view of the case with the sting behind the ball, it means that either the natural preferred vortex pair orientation is downward for this ball orientation, or that the sting being behind the ball also has a downward locking effect. The fact that the lift magnitude is much smaller for the sting-behind-the-ball case could mean there are potentially some vortex pair rotations, with the downward orientation being the most frequent one. In case there are, it seems likely that the sting from behind has a limited effect. In case there are not, the question of the effect of the sting remains open.

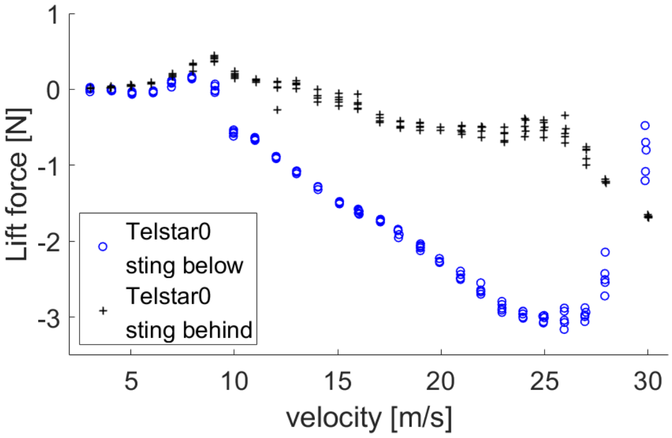

Figure 5.20: Balance measurements lift versus velocity of the Telstar 0° case, for stings from below and behind.

An attempt was made to investigate further how much difference is in the wake flow between having the sting below or behind. With no PTV data for the case with the sting from behind, this was done by comparing the full instantaneous data of the balance measurements of both cases. Figures 5.21a-c show the periodograms of both cases for the measured drag, side and lift forces at 22 m/s. This velocity was chosen because it is in the supercritical regime, and the mean side forces are almost the same.

What can be seen is that there are peaks mostly at the same frequencies, so at least the position of the sting does not entirely change the flow around the ball. The similarities are seen for frequencies of 10 Hz and higher. These peaks are likely due to vibrations of the stings, as also supported by subfigures d-f, which show the same periodograms of only the stings. The same peaks in these figures can be seen as the peaks in the periodograms with the balls.

Considering again subfigures a-c, for the frequencies below 10 Hz, there are some minor differences in peaks. These likely point to differences in the flows for both cases. Whether there are rotations of the wake vortex pair for the case with the sting from behind cannot be said with the current available information. There are however no clear indications for them, which would for example be things such as low frequency peaks and similarity in those for the lift and side forces.

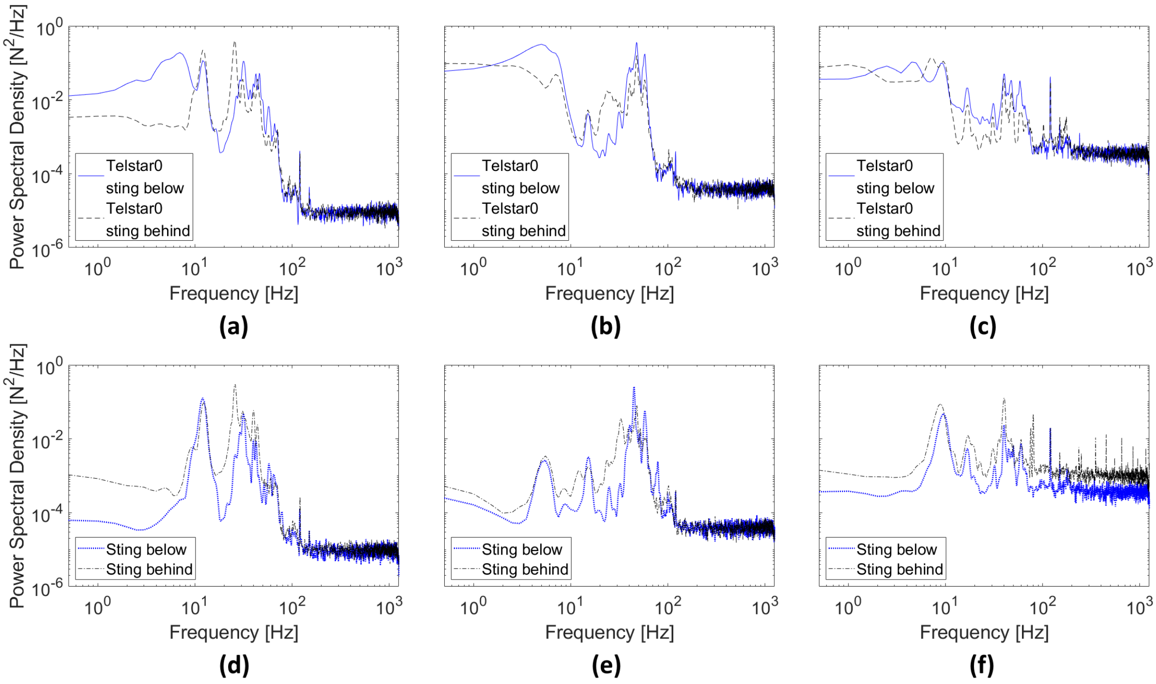

Figure 5.21: **(a-c)** Periodograms of the instantaneous balance measurements at 22 m/s for the Telstar at 0° orientation with stings from below and behind, for drag, sideforce and lift respectively. **(d-f)** Same periodograms for only the stings.

5.4. Trajectory simulation

Trajectory simulations were made for shots of 25 m from the goal with initial velocities of 30 m/s and launch angles of 16°. The results are shown in Figs. 5.22 and 5.23, which are a 3D overview and a top view. The x direction is towards the goal, the balls are shot from (0,0,0) and the goal plane lies at x = 25 m. All balls end up just below the bar. However, large differences in sideways movement can be seen, which stresses the importance of orientations on the trajectory of the balls. For the Telstar, the final difference between the two orientations considered is more than 1 m, and for the World Cup ball the difference is over 0.5 m. Both are large enough to affect whether the shot is promoted to a goal or not, considering that the distance of 25 m is travelled in just over 1 second.

Interesting to note is that the difference in lateral displacement between the two orientations of the World Cup ball is actually smaller than between the difference between the two orientations of the Telstar ball. This may not be expected at first thought, but it should be realised that the ball decelerates throughout its flight. At lower velocities the difference in side force between the two orientations is not that large while they are still moving apart and there is a point where they cross. In case of the Telstar ball, a larger difference between the sideforces of both orientations remains while decelerating. Notice also that the changing signs while decelerating also causes a knuckleball effect for the World Cup ball at 0° orientation.

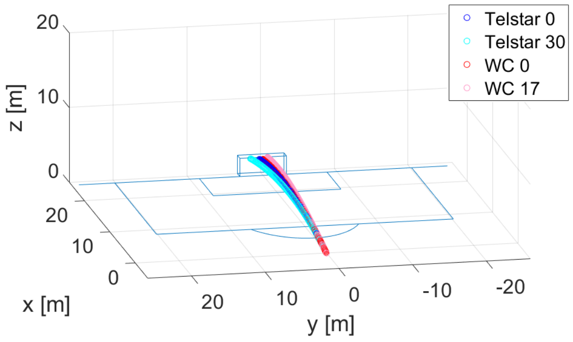

Figure 5.22: 3D view of trajectory simulations of shots 25 m from the goal with initial velocities of 30 m/s and launch angles of 16°.

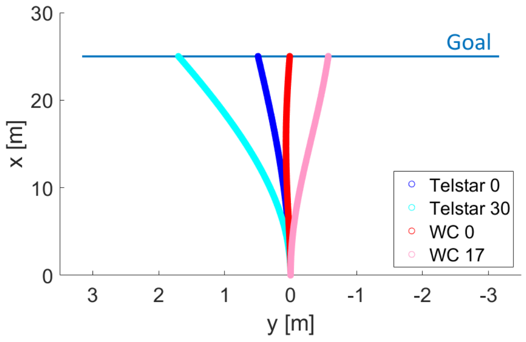

Figure 5.23: Top view of trajectory simulations of shots 25 m from the goal with initial velocities of 30 m/s and launch angles of 16°.

6

Conclusions and Recommendations

The robotic PTV system of the TU Delft has been used to take measurements of the wake flows of footballs, to prove its suitability as a future tool for design or certification of footballs. From the results of the experiments performed, the five questions posed to assess achievement of the research objective could be answered.

First, it has been shown sufficient spatial resolution can be achieved in the entire wake of a football by ensemble averaging multiple runs. Differences in the wakes for the subcritical, critical and supercritical *Re* regimes could be seen clearly, with large wakes in the subcritical regimes and small wakes in the supercritical regimes. Also, the separation angles found from the measurements match those of literature.

In principle, also differences in the wakes for different footballs or football orientations could be discerned. However, in practice there were barely differences between the wakes and only one case proved this point. The reason why there were hardly differences between the cases is discussed in a later paragraph on limitations. Related to that discussion is also the answer to the second question, whether the vortex pairs could be seen from the data. They could, which is positive, but they did not seem to rotate at all, which was however what was expected from literature. Therefore they had a very pronounced orientation even in the time-averaged data. This issue is related to the why there are hardly any differences between the cases.

The third question concerned validation of these PTV measurements. The results seemed to be in good agreement with the balance measurements. When a wake was seen to be deflected in a certain direction on the PTV results, a force to the opposite direction of this induced velocity was to be expected. This was always the case when comparing them to the balance measurements. Therefore, this question can also be answered positively.

The versatility of the system questioned fourthly was also confirmed. The whole system was set up and fixed without moving during the whole experimental campaign, and geometrical calibration was also performed only once then. An entire wake could be captured as sufficient data could be retrieved using the system. Important factor was the robotic arm, with which the cameras could be moved.

The last question to be tested was that the system had to be non-intrusive and not influence the flow structures measured. It was concluded that this was not a problem, by comparing data from PTV measurements taken from different locations. Also, when comparing the measurements to the results from the balance measurements where the acquisition system is entirely retracted, it can be seen that the wakes are deflected in the same directions. It is possible to conduct an additional test by imaging the wake with the setup alternately on both sides of the football and compare the results, but this is deemed not necessary.

All in all, all the questions have been answered positively and as such the system in itself can be concluded to be suitable for the desired purpose. There is however a large issue that came up from the results. The setup for fixing the footballs used a sting below the footballs to which they were attached. This was to conveniently test multiple orientations. However, it seemed that this influenced the flow behind a ball, drawing the wake into one certain direction. This became more apparent after a comparison of balance measurements data of a setup where the sting was placed from behind the ball, although there were no PTV measurements for that. This limitation will have to be solved, or else the use of this system will be irrelevant for the intended purpose of studying the flow characteristics of footballs.

A solution could therefore be to use a setup with the sting from behind the balls, with the drawbacks of less convenient orientations sweep and having a sting in the region of interest when imaging in the wake.

Also, it was not clear from the data currently available whether the issue that arose with the sting from below was solved in case the sting was from behind, or whether it only alleviated the issue.

Therefore, the following recommendations are made for further investigation. The first thing that can be done, is to test whether taking measurements with the sting behind the ball is a proper solution. It is expected that even if the wake vortex pair has a preferred orientation, there should still be some rotations. This could be quickly investigated as a first step, using just planar PIV/PTV in the wake. In case the expectations are confirmed, it could then be taken a step further and the robotic system can be used to determine whether it is able to capture the desired results when there is a sting in the wake.

If however the wake seems to be fixed still, it could mean two things. Either the setup with the sting from behind still has a large influence on the flow in the wake of a football, or the locking from the vortex pair is due to the surface pattern of the football. If it is the latter, then again one can proceed with testing the volumetric PTV using the robotic system. To find out which is the case, there are two options. Repeat the measurements with a smooth sphere, or test the football in a measurement without a sting at all and then compare the results. This could be achieved using for example a kicking robot combined with the 'Ring of Fire' [43], another large scale PIV system of the TU Delft in which a moving object passes through a volume of seeding (HFSB). The challenge with this is however that the ball passes quickly through the measurement volume, making it more difficult to obtain enough data. Also, it may not be guaranteed that the ball orientation achieved is the same every time. However, if it is shown that even with a sting from behind the setup has too much influence on the flow, this 'Ring of Fire' system will be the only remaining option for volumetric quantification of the wake flow of footballs.

A

Ball-sting Interface Bowl

In this Appendix, a few more details are provided about the ball-sting interface bowl, which was shortly introduced in Chapter 4. The following topics are discussed: the design process in Sec. A.1, manufacturing in Sec. A.2 and testing in Sec. A.3. Figure A.3 shows the technical drawings of the bowl. As the complex curved outer surface cannot be properly depicted, the five control points (CP) used to describe the spline are shown in red in the section view, as well as the origin that is defined at the end of the internal shaft in the symmetry plane. Table A.1 lists the locations of the control points with respect to the origin and the curvature radii at those points.

A.1. Design process

A large number of designs with varying shapes and sizes had been produced and tested, before the one in use currently was accepted. Previous designs were discarded for one or more of the following reasons: insufficient stiffness, insufficient strength, incorrect radius of curvature and inadequate edge thickness.

Insufficient stiffness would lead to too large vibrations, which would disturb the measurements. Three regions of problematic behaviour were: connection between ball and bowl, stiffness of the bowl itself and connection between bowl and sting. The stiffness of the connection between ball and bowl was mainly influenced by the size of the bowl. For this, a trade-off had to be made between the stiffness and the interference of the bowl with the flow. Eventually, a size was chosen such that the bowl fits nicely inside a panel of the Telstar ball, for smooth transitions all around from ball to bowl. An asymmetric bowl elongated towards the wake side of the ball was considered, but discarded because this would make flexible research of multiple ball orientations impossible.

The stiffness of the bowl itself was increased by increasing thickness of the centre part of the bowl until the bowl could barely be bent by hand. The edges had to stay thin to transition smoothly into the football.

To achieve stiffness between the bowl and the sting, a foot in which the sting could be inserted was added. It seems obvious that there should be a foot to insert the sting, but the reason that at first there was not, was that the bowl was also designed for another attachment method to the ball, a method where the sting was also attached differently to the bowl. For the current method, it is indeed essential, and sufficient stiffness was achieved by making the foot long enough.

Another point of consideration was that the bowl had to be strong enough to withstand the forces during testing, and also that the connection between ball and bowl had to hold. For the first, it meant increasing the fill rate of the 3D-printing and the thickness of the foot. For the latter, it meant that eventually it was decided to use epoxy resin. These strengths were tested and passed, discussed in Sec. A.3.

Next, the radius of curvature of the upper surface of the bowl had to match that of the outer surfaces of the footballs. Actually, slightly smaller such that there was some space between the ball and bowl for the epoxy resin. Multiple prototypes were produced to match these surfaces. Just using the measured diameter to obtain the radius of curvature did not suffice, as the bowls initially had too large of a radius of curvature. This could perhaps be due to imperfect sphericity of the balls, or inaccurate 3D-printing.

A final issue that arose was a practical manufacturing issue. The edge of the bowl had to be designed with sufficient thickness, which means that in vertical direction it had to be at least the layer thickness of the 3D-printing. Otherwise the edge would end up being jagged.

A.2. Manufacturing

The bowl was manufactured using 3D-printing, because this allowed to rapidly, easily and cheaply create multiple prototypes. Using a lathe to create it manually was not even possible due to the complex shape. The final product could have been made then from metal using a CNC machine, but this was not necessary because the 3D-printed part met the requirements, and so worrying about generating the proper code for the CNC machine could also be avoided.

The 3D-printing was done using PLA as material. The infill density was set to 100% to achieve higher strength and printing of support material was enabled because there was no flat surface to position it on without having overhang. The part had to be printed upside-up. Otherwise, although a smooth outer surface would be achieved, the support material could not be properly removed from the concave part, which was essential for attaching to the ball. The support material from the outer convex part was removed afterwards using pliers (safer than cutting) and sanding to create a smooth outer surface.

A.3. Testing

To test whether the strength of the bowl and its connection were strong enough, some tests were performed in the smaller W-tunnel of the HSL. A football was attached to the bowl which was placed on a sting, just like they would in the eventual experiments, and held in the jet of the wind tunnel. During the first series of tests, the bowl broke at the location where the foot merges into the curved shape at around $23 m/s$ wind speed. Also, it appeared the connection made at first using double-sided tape was not very secure and seemed to want to come loose, though it never did before breaking. From these tests, it was decided to increase thickness of the foot, use 100% infill and epoxy resin for the connection to the ball to be safer.

A second test series was performed using epoxy resin for the connection. The bowl was tested until $26 m/s$ and did not break. At this point the improved bowls were not ready yet, but due to this result it was assumed that using those in combination with epoxy resin connections, there would be no problems when experimenting until $30 m/s$. Figures A.1 and A.2 show testing of the bowl and a broken bowl from the first tests.

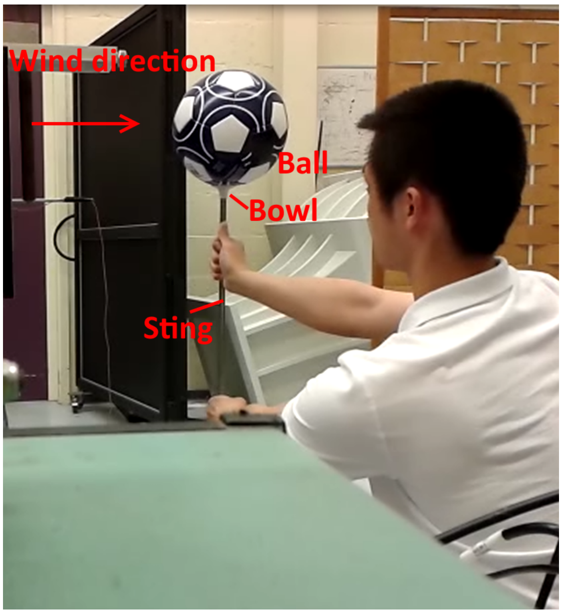

Figure A.1: Testing of strength of ball-sting interface bowl.

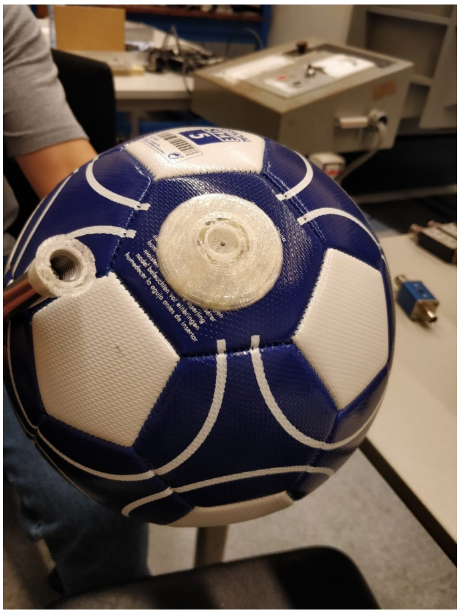

Figure A.2: A broken bowl from the first bowl strength tests.

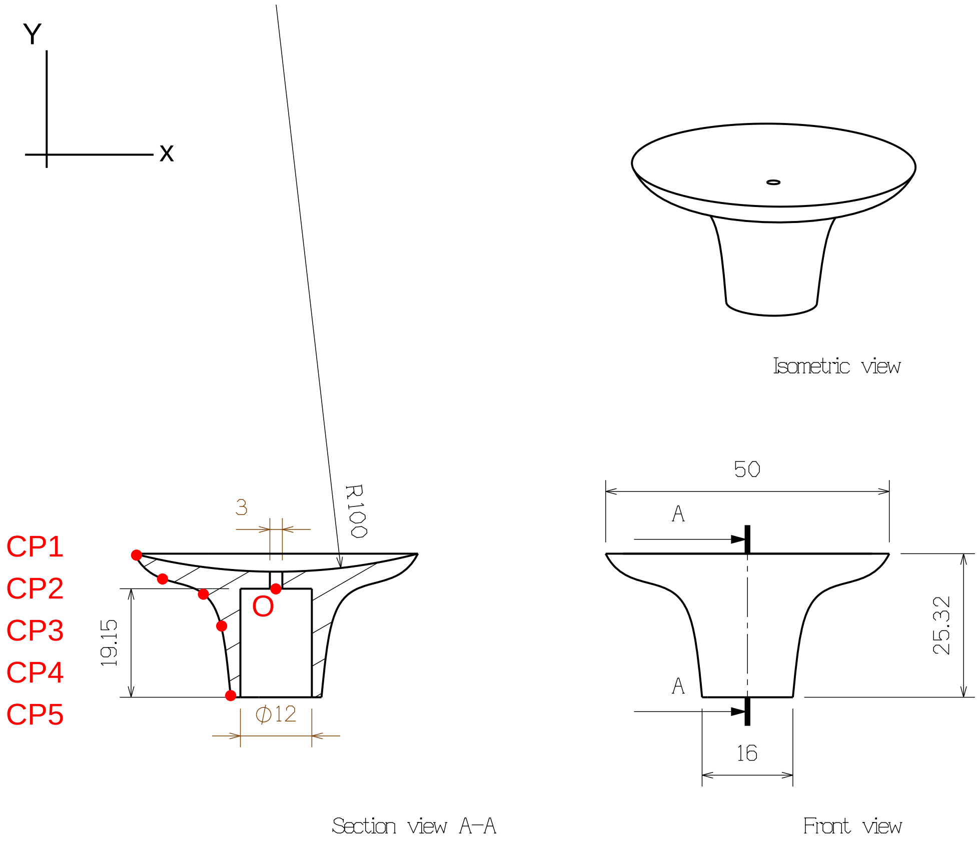

Figure A.3: Technical drawings of the ball-sting interface bowl. Scale 1:1.

Table A.1: Control points defining the spline that describes the outer double-curved surface of the ball-sting interface bowl.

Control point	**X-coordinate [mm]**	**Y-coordinate [mm]**	**Curvature radius [mm]**
CP1	-25	6.175	11.065
CP2	-20.325	1.883	12.127
CP3	-12.942	-0.811	-6.664
CP4	-9.685	-6.645	-25.012
CP5	-8	-19.174	-328.125

Bibliography

[1] Achenbach E. "Experiments on the flow past spheres at very high Reynolds numbers". *J. Fluid Mech.*, Vol. 54, part 3, 1972. pp. 565 - 575.

[2] Achenbach E. "Vortex shedding from spheres". *J. Fluid Mech.*, Vol. 62, part 2, 1974. pp. 209 - 221.

[3] Adidas. "History of adidas World Cup Match Balls". `https://news.adidas.com/us/Lookbooks/history-of-adidas-world-cup-balls/s/46506801-f5d9-4a51-b5be-c04557c59caf`. Accessed online 2018-7-15.

[4] Alam F., Chowdhury H., Moria H. and Fuss F.K. "A Comparative Study of Football Aerodynamics". *Procedia Engineering*, Vol. 2, 2010. pp. 2443 - 2448.

[5] Alam F., Chowdhury H., Moria H., Fuss F.K., Khan I., Aldawi F. and Subic A. "Aerodynamics of contemporary FIFA soccer balls". *Procedia Engineering*, Vol. 13, 2011. p. 188 - 193. DOI: 10.1016/j.proeng.2011.05.071.

[6] Alons H.J., Nationaal Lucht- en Ruimtevaartlaboratorium. "OJF External Balance - Documentation". NLR-CR-2008-695.

[7] Asai T. and Kamemoto K. "Flow structure of knuckling effect in footballs". *Journal of Fluids and Structures*, Vol. 27, Issues 5-6, 2011. pp. 727 - 733. DOI: 10.1016/j.jfluidstructs.2011.03.016.

[8] Asai T., Hong S., Kimachi K., Abe K., Kai H. and Nakamura A. "Flow Visualisation around Spinning and Non-Spinning Soccer Balls Using the Lattice Boltzmann Method". *Proceedings*, Vol. 2, Issue 6, 2018. p. 237. DOI: 10.3390/proceedings2060237.

[9] Asai T., Seo K., Kobayashi O. and Sakashita R. "Fundamental aerodynamics of the soccer ball". *Sports Engineering*, Vol. 10, 2007. pp. 101 - 110. DOI: 10.1007/BF02844207.

[10] Asai T., Seo K., Sakurai Y., Ito S., Koike S., Murakami M. . "A Study of Knuckling Effect of Soccer Ball (P106)". *The Engineering of Sport 7*, 2008. pp. 555 - 562. DOI:10.1007/978-2-287-09411-8$_6$5.$Springer, Paris$.

[11] Barber S. and Carré M.J. "The effect of surface geometry on soccer ball trajectories". *Sports Engineering*, Vol. 13, Issue 1, 2010. pp. 47 - 55. DOI: 10.1007/s12283-010-0048-x.

[12] Barber S., Chin S.B. and Carré M.J. "Sports ball aerodynamics: A numerical study of the erratic motion of soccer balls". *Computers and Fluids*, Vol. 38, Issue 6, 2009. p. 1091 - 1100. DOI: 10.1016/j.compfluid.2008.11.001.

[13] Barber S., Haake S.J. and Carré M.J. "Using CFD to Understand the Effects of Seam Geometry on Soccer Ball Aerodynamics". *The Engineering of Sport 6*, 2006. Springer, New York, NY. DOI: 10.1007/978-0-387-46051-2$_2$3.

[14] Carré M.j., Asai T., Akatsuka T. and Haake S.J. "The curve kick of a football II: flight through the air". *Sports Engineering*, Vol. 5, Issue 4, 2002. p. 193 - 200. DOI: 10.1046/j.1460-2687.2002.00109.x.

[15] Carré M.J., Goodwill S.R. and Haake S.J. "Understanding the effect of seams on the aerodynamics of an association football". *Proceedings of the Institution of Mechanical Engineers, Part C: Journal of Mechanical Engineering Science*, Vol. 219, Issue 7, 2005. pp. 657 - 666. DOI: 10.1243/095440605X31463.

[16] Elsinga G.E., Scarano F., Wieneke B. and van Oudheusden B.W. "Tomographic particle image velocimetry". *Exp Fluids*, Vol. 41, Issue 6, 2006. pp. 933-947. DOI: 10.1007/s00348-006-0212-z.

[17] FIFA. "Footballs testing manual 2018". `https://football-technology.fifa.com/en/media-tiles/footballs-testing-manual-2018/`. Accessed online 2018-7-15.

[18] Goff J.E. and Carré M.J. "Trajectory analysis of a soccer ball". *American Journal of Physics*, Vol. 77, Issue 11, 2009. p. 1020. DOI: 10.1119/1.3197187.

[19] Goff J.E., Asai T. and Hong S. "A comparison of Jabulani and Brazuca non-spin aerodynamics". *Proceedings of the Institution of Mechanical Engineers, Part P: Journal of Sports Engineering and Technology*, Vol. 228, Issue 3, 2014. pp. 188 - 194. DOI: 10.1177/1754337114526173.

[20] Goff J.E., Hong S. and Asai T. "Aerodynamic and surface comparisons between Telstar 18 and Brazuca". *Proceedings of the Institution of Mechanical Engineers, Part P: Journal of Sports Engineering and Technology*, 2018. pp. 1 - 7. DOI: 10.1177/1754337118773214.

[21] Goff J.E., Kelley J., Hobson C.M., Seo K., Asai T. and Choppin S.B. "Creating drag and lift curves from soccer trajectories". *European Journal of Physics*, Vol. 38, Issue 4, 2017. DOI: 10.1088/1361-6404/aa6fcd.

[22] Goff J.E., Smith W.H. and Carré M.J. "Football boundary-layer separation via dust experiments". *Sports Engineering*, Vol. 14, Issue 2-4, 2011. pp. 139 - 146. DOI: 10.1007/s12283-011-0074-3.

[23] Hong S. and Asai T. "Aerodynamic effects of dimples on soccer ball surfaces". *Heliyon*, Vol. 3, Issue 10, 2017. DOI: 10.1016/j.heliyon.2017.e00432.

[24] Hong S., Asai T. and Seo K. "Visualization of air flow around soccer ball using a particle image velocimetry". *Scientific Reports*, Vol. 5, 2015. Article 15108. DOI: 10.1038/srep15108.

[25] Hong S., Chung C., Nakayama M., Asai T. "Unsteady Aerodynamic Force on a Knuckleball in Soccer". *Procedia Engineering*, Vol. 2, Issue 2, 2010. pp. 2455 - 2460. DOI: 10.1016/j.proeng.2010.04.015.

[26] Ifeachor E.C. and Jervis B.W. *"Digital Signal Processing: A Practical Approach. Second edition"*. Pearson Education Limited Harlow, 2002. ISBN-10: 0-201-59619-9. ISBN-13: 978-0-201-59619-9.

[27] Ito S., Kamata M., Asai T. and Seo K. "Factors of unpredictable shots concerning new soccer balls". *Procedia Engineering*, Vol. 34, 2012. pp. 152 - 157. DOI: 10.1016/j.proeng.2012.04.027.

[28] Jux C. MSc Thesis "Robotic Volumetric Particle Tracking Velocimetry by Coaxial Imaging and Illumination". 2017. `https://repository.tudelft.nl/islandora/object/uuid%3Ad5947c06-2be2-4ad3-aa9f-4c012fa54f0b?collection=education`. Accessed online 2018-10-23.

[29] Mizota T., Kurogi K., Ohya Y., Okajima A., Naruo T. and Kawamura Y. "The strange flight behaviour of slowly spinning soccer balls". *Scientific Reports*, Vol. 3, 2013. Article 1871. DOI: 10.1038/srep01871.

[30] Murakami M., Seo K., Kondoh M. and Iwai Y. "Wind tunnel measurement and flow visualisation of soccer ball knuckle effect". *Sports Engineering*, Vol. 15, Issue 1, 2012. pp. 29 - 40. DOI: 10.1007/s12283-012-0085-8.

[31] Nishino K., Kasagi N. and Hirata M. "Three-Dimensional Particle Tracking Velocimetry Based on Automated Digital Image Processing". *Journal of Fluids Engineering*, Vol. 111, Issue 4, 1989. DOI: 10.1115/1.3243657.

[32] Oggiano L. and Saetran L. "Aerodynamics of modern soccer balls". *Procedia Engineering*, Vol. 2, 2010. pp. 2473 - 2479.

[33] Passmore M.A., Rogers D., Tuplin S., Harland A., Lucas T. and Holmes C. "The aerodynamic performance of a range of FIFA-approved footballs". *Proceedings of the Institution of Mechanical Engineers, Part P: Journal of Sports Engineering and Technology*, Vol. 226, Issue 1, 2012. pp. 61 - 70. DOI: 10.1177/1754337111415768.

[34] Passmore M.A., Tuplin S., Spencer A. and Jones R. "Experimental studies of the aerodynamics of spinning and stationary footballs". *Proceedings of the Institution of Mechanical Engineers, Part C: Journal of Mechanical Engineering Science*, Vol. 222, Issue 2, 2008. pp. 195 - 205. DOI: 10.1243/09544062JMES655.

[35] Present Press B.V. "The Open Jet Facility". `https://d1rkab7tlqy5f1.cloudfront.net/LR/Organisatie/Afdelingen/Aerodynamics__Wind_Energy__Flight_Performance_and_Propulsion/OJF_boek.pdf`. Accessed online 2018-9-20.

[36] Raffel M., Willert C.E., Wereley S.T. and Kompenhans J. *"Particle Image Velocimetry - A Practical Guide. Second edition".* Springer Berlin Heidelberg New York, 2007. ISBN: 978-3-540-72307-3.

[37] Ragni D., Schrijer F., van Oudheusden B.W. and Scarano F. "Particle tracer response across shocks measured by PIV". *Exp Fluids*, Vol. 50, Issue 1, 2011. pp. 53-64. DOI: 10.1007/s00348-010-0892-2.

[38] Scarano F. "Tomographic PIV: principles and practice". *Meas. Sci. Technol.*, Vol. 24, Issue 1, 2013. DOI: 10.1088/0957-0233/24/1/012001.

[39] Scarano F., Ghaemi S., Caridi G.C.A., Bosbach J., Dierksheide U. and Sciacchitano A. "Shake-The-Box: Lagrangian particle tracking at high particle image densities". *Exp Fluids*, Vol. 56, Issue 42, 2015. DOI: 10.1007/s00348-015-1909-7.

[40] Schanz D., Gesemann S. and Schröder A. "Shake-The-Box: Lagrangian particle tracking at high particle image densities". *Exp Fluids*, Vol. 57, Issue 70, 2016. DOI: 10.1007/s00348-016-2157-1.

[41] Schneiders J.F.G., Scarano F., Jux C. and Sciacchitano A. "Coaxial volumetric velocimetry". *Meas. Sci. Technol.*, Vol. 29, Issue 6, 2018. DOI: 10.1088/1361-6501/aab07d.

[42] Sciacchitano A. and Scarano F. "Elimination of PIV light reflections via a temporal high pass filter". *Meas. Sci. Technol.*, Vol. 25, 084009, 2014. DOI: 10.1088/0957-0233/25/8/084009.

[43] Spoelstra A.M.C.M.G. MSc Thesis "Aerodynamics of transiting objects via large-scale PIV - the Ring of Fire Concept". 2017. `https://repository.tudelft.nl/islandora/object/uuid%3A73bcc7a8-68b9-4e5b-b79a-65f41fc45bbb`. Accessed online 2018-11-09.

[44] Taneda S. "Visual observations of the flow past a sphere at Reynolds numbers between 10^4 and 10^6. *J. Fluid Mech.*, Vol. 85, part 1, 1978. pp. 187 - 192.

[45] Universal Robots. "UR5 Technical details". `https://www.universal-robots.com/media/1801303/eng_199901_ur5_tech_spec_web_a4.pdf`. Accessed online 2018-11-5.

[46] Welch P. "The use of fast Fourier transform for the estimation of power spectra: A method based on time averaging over short, modified periodograms". *IEEE Transactions on Audio and Electroacoustics*, Vol. 15, Issue 2, 1967. pp. 70-73. DOI: 10.1109/TAU.1967.1161901.

[47] Wieneke B. "Iterative reconstruction of volumetric particle distribution". *Meas. Sci. Technol.*, Vol. 24, 024008, 2013. DOI: 10.1088/0957-0233/24/2/024008.